Bridging Ion and Neutron Irradiation: A Predictive Framework for Swelling in Structural Alloys

Denghuang Chen,[1,*] Wei Ge,[1,*] Fengping Luo,[1,*] Jia Huang,[2] Guo Li,[1] Zhiying Gao,[1] Jin Wang,[1] Bowen Zhang,[1] Yuxing Liu,[1] Shijun Zhao,[3] Haocheng Liu,[1] Steven J. Zinkle,[4] Yugang Wang,[1,†] and Chenxu Wang[1,‡]

[1]*State Key Laboratory of Nuclear Physics and Technology, School of Physics, Peking University, 100871, Beijing, China*
[2]*School of Materials Science and Engineering, Shanghai Jiao Tong University, 200240, Shanghai, China*
[3]*Department of Mechanical Engineering, City University of Hong Kong, Hong Kong, China*
[4]*Department of Nuclear Engineering, University of Tennessee, Knoxville, Tennessee, 37996, USA*

(Received 28 January 2026; revised 20 May 2026; accepted 15 June 2026; published 7 July 2026)

Advanced nuclear energy systems critically rely on the irradiation tolerance of structural materials in the reactor core. However, quantitatively predicting reactor-relevant, high-dose neutron swelling from low-dose neutron data or high-dose-rate heavy-ion irradiation experiments remains a long-standing challenge. Existing approaches are often case-specific, requiring neutron–ion benchmarking and substantial empirical tuning. Here we derive a quantitative, physically grounded relationship linking cavity swelling to both dose and dose rate at a fixed temperature, combining cluster-dynamics insights—particularly dose-rate-enhanced defect nucleation—with simplified rate-equation analysis. Validation across extensive literature data demonstrates that the proposed relationship is broadly applicable across major classes of structural alloys and irradiation conditions, accurately capturing the nonlinear dose dependence of swelling and its systematic variation with dose rate. It thereby enables the prediction of high-dose swelling behavior from low-dose data, defines an equivalent dose that produces the same swelling level across different dose rates, and provides a quantitative basis for comparing swelling resistance across materials, independent of specific material systems or irradiation conditions. Furthermore, ion-irradiation experiments demonstrate that, using ion data alone, the relationship enables quantitative prediction of neutron-irradiation swelling across an ion–neutron dose-rate gap spanning several orders of magnitude. This work provides a practical and predictive framework for evaluating irradiation-induced swelling in structural materials, offering a quantitative pathway to bridge ion and neutron irradiation experiments at high irradiation doses and supporting materials development and safety evaluation for advanced nuclear energy systems.

DOI: 10.1103/fsh5-qg22

I. INTRODUCTION

The economics, safety, and lifetime of nuclear reactors critically depend on the durability of structural materials operating in reactor cores, where components are exposed to intense neutron irradiation reaching damage levels of hundreds of displacements per atom (dpa) [1–3]. In parallel with the development of advanced nuclear energy systems, the extension of service lifetimes for existing reactors further amplifies the demand for reliable assessment of material degradation under prolonged neutron irradiation [4]. A central challenge is therefore to quantitatively evaluate and predict irradiation-induced degradation at reactor-relevant doses, where direct experimental access is limited.

Among various irradiation-induced degradation mechanisms—including hardening, embrittlement, and phase instability [5]—volume swelling plays a particularly critical role, as it directly limits dimensional stability and component lifetime [6,7]. While swelling often exhibits an approximately linear dependence on dose at sufficiently high damage levels [8], its evolution over the full dose range is intrinsically nonlinear, progressing through incubation, transient growth, and steady-state regimes. During incubation, swelling remains negligible despite accumulating damage, followed by rapid growth once stable cavities form. Although the nonlinear dose dependence

*These authors contributed equally to this work.
†Contact author: ygwang@pku.edu.cn
‡Contact author: cxwang@pku.edu.cn

of swelling has been elucidated under electron irradiation in our previous study [9], for reactor-relevant neutron environments, a quantitative and physically grounded relationship that captures swelling as a function of irradiation dose across these regimes remains lacking, severely limiting predictive capability.

This limitation is exacerbated by practical constraints associated with neutron irradiation experiments. Achieving lifetime-relevant doses in test reactors typically requires irradiation campaigns lasting more than a decade, accompanied by high cost, long turnaround times, and substantial radioactivation. As a result, heavy-ion irradiation has become a widely used surrogate technique, enabling rapid exploration of irradiation effects—including cavity swelling—via transmission electron microscopy (TEM) [8,10–14]. However, ion irradiation is conducted at dose rates that are typically three to four orders of magnitude higher than those of neutron irradiation, and numerous experiments have demonstrated that swelling is strongly dose-rate dependent, with higher dose rates generally producing lower swelling levels under otherwise similar conditions [5,10,11,15–17]. Despite its practical advantages [5,16,18–21], this pronounced dose-rate disparity raises fundamental questions about the quantitative representativeness of ion-irradiation results for reactor-relevant neutron conditions. Because our previous model [9] was developed for constant dose-rate conditions, it cannot bridge this massive dose-rate gap, where extreme variations in defect production fundamentally alter the nucleation density of irradiation-induced sinks. In particular, two unresolved challenges continue to limit materials evaluation: (i) whether high-dose neutron irradiation swelling can be reliably predicted from low-dose neutron irradiation data and (ii) how swelling under low-dose-rate neutron irradiation can be quantitatively inferred from high-dose-rate ion irradiation experiments. Addressing these challenges requires a framework that explicitly links swelling to both irradiation dose and dose rate.

At the microstructural level, volumetric swelling originates from the accumulation and growth of irradiation-induced cavities formed through the production, migration, and aggregation of point defects generated by displacement cascades [8]. Although neutrons and ions differ in mass, charge, and primary damage characteristics, similar classes of irradiation-induced microstructures—including dislocation loops and cavities—are widely observed in both cases [5,8]. Importantly, swelling develops over relatively large spatial and temporal scales, suggesting that long-term defect kinetics, rather than the detailed morphology of individual cascades, play a dominant role in controlling macroscopic swelling behavior. Consistent with this perspective, our previous object kinetic Monte Carlo (OKMC) simulations demonstrated that differences in irradiation dose rate dominate swelling behavior, while cascade-related differences between ions and neutrons play a secondary role [22]. This observation motivates the development of rate-theory-based descriptions that emphasize defect production and evolution over extended timescales. Moreover, volumetric swelling provides a direct quantitative bridge between microstructural cavity distributions and macroscopic dimensional change, making it a particularly suitable quantity for establishing equivalence relations across irradiation conditions.

Substantial efforts have been devoted to understanding irradiation effects across different doses and dose rates. A long-standing strategy for correlating high-dose-rate ion irradiation with reactor neutron irradiation is the temperature-shift concept rooted in Mansur's invariance theory [23], which posits that raising the irradiation temperature can offset dose-rate effects. Based on vacancy migration and formation energetics, it predicts a temperature increase of $\sim$120 °C for ferritic–martensitic steels under representative ion–neutron dose-rate disparity [24]. Yet experimental realizations vary widely: neutron-like cavity swelling has been reported with only a 17°C shift when coupled with $\sim$1 appm He preimplantation [25], whereas other work requires a 70°C shift and, under dual-beam conditions, substantially elevated He injection rates [24]; notably, a recent study suggests that even single-ion irradiation can reproduce neutron-like cavity size and number density with a 70°C shift [26]. For austenitic alloys, the closest agreement has even been obtained only when the He/dpa ratio in dual-ion irradiation is reduced well below the neutron value [27]. Together, these studies demonstrate that, with carefully selected irradiation parameters, ion irradiation reproduces neutron-like swelling behavior within the invariance-theory framework [16], but the required parameter combination remains highly case-specific and typically depends on direct neutron-to-ion benchmarking. As a result, achieving quantitative agreement typically relies on extensive trial-and-error exploration within a high-dimensional parameter space, rather than on a predictive relationship that can be applied a priori.

This limitation reflects a broader challenge in bridging irradiation modalities. Achieving true predictive capability across dose rates requires an explicit, quantitative description of how swelling depends on dose rate itself, rather than compensating for dose-rate effects through adjustments of irradiation parameters. Meanwhile, mesoscale simulation techniques—including cluster dynamics (CD), OKMC, and phase-field modeling—have advanced mechanistic understanding of irradiation-induced defect evolution [8,28–31]. However, their direct quantitative application to engineering alloys remains challenging due to uncertainties in material-specific parameters and the difficulty of representing complex microstructural sink structures with sufficient fidelity.

Motivated by these limitations and to advance beyond single-state dose scaling [9], we establish here a generalized quantitative relationship that explicitly couples cavity swelling to both irradiation dose and dose rate at a fixed temperature. The framework combines essential physical insights from CD simulations—most notably dose-rate-enhanced defect nucleation—with simplified rate-equation analysis. Higher dose rates increase the concentration of mobile defect clusters, promoting the nucleation of irradiation-induced defects and systematically modifying cavity growth kinetics. By incorporating this dose-rate dependence explicitly, the resulting relationship provides a physically interpretable description of swelling across irradiation conditions.

The proposed relationship is validated against extensive experimental data [11,17,4,32–46] spanning a wide range of alloys, doses, and dose rates, demonstrating its ability to capture both nonlinear dose dependence and systematic dose-rate effects. The success of a single functional form across these diverse alloy systems indicates that the framework has broad applicability to structural materials and that its fitted parameters can serve as quantitative descriptors for comparing swelling resistance across materials. Furthermore, ion-irradiation experiments on pure nickel are used to demonstrate predictive capability: using ion data alone, swelling under neutron irradiation conditions at the same temperature is successfully predicted despite a dose-rate difference of approximately four orders of magnitude. The resulting agreement with independent neutron-irradiation data confirms that the established relationship provides a practical and quantitatively testable framework for correlating swelling across irradiation modalities. This framework enables accelerated materials screening and performance evaluation, offering a predictive pathway essential for the development and qualification of structural materials for advanced nuclear energy systems.

II. METHODS

A. Cluster dynamics simulations

CD models microstructural evolution under irradiation by tracking defect cluster aggregation via coupled rate equations. These equations govern the time-dependent concentrations of defects (e.g., interstitials and vacancies) across size regimes, where cluster growth and dissociation are controlled by the absorption of mobile defect clusters—including point defects—and by point-defect emission. Rate constants are determined by irradiation conditions (e.g., dose rate and temperature) and material properties (e.g., migration barriers and binding energies). The framework's theoretical foundations and computational implementation are well-established in prior studies [29,47–52]. In this work, CD simulations were performed for pure iron and pure nickel systems and further extended to a model ferritic alloy, Fe–9Cr. Table I summarizes the fundamental parameters employed in the CD simulations for iron and nickel, including cascade properties, defect characteristics, and material-specific properties. In the Fe–9Cr CD simulations, the effect of Cr on vacancy-cluster properties is assumed to be negligible [53]; therefore, all vacancy-cluster parameters are taken to be the same as in pure Fe. Cr is incorporated only through its impact on SIA-cluster mobility: the SIA-cluster diffusivity is calculated using the expressions in Ref. [53], Table I. Molecular dynamics simulations were performed using LAMMPS [54] to investigate cascade evolution in pure nickel systems. The interatomic interactions were described by the EAM potential [55], a primary knock-on atom energy of 25 keV was selected.

The CD simulations track the evolution of both vacancy-type clusters (V_y, $y \leqslant N$) and interstitial-type clusters (I_p, $p \leqslant N$) through individual rate equations. For larger defect clusters ($y > N, p > N$), the Fokker–Planck (FP) approximation is implemented to describe their evolution [49,56]. Vacancy-type clusters induced by irradiation are modeled as spherical cavities, while interstitial-type clusters are represented as dislocation loops with a discoid morphology [30,47]. The FP approximation treats the defect cluster concentration $C_v(y)$ as discrete values evaluated at grid points $y = Y$ within the size space. By performing a second-order Taylor expansion of $C_v(y)$ around each grid point and

TABLE I. Parameters employed in the CD simulations.

Symbol	Description	Value in iron	Value in nickel
a_0	Lattice parameter (nm)	0.287	0.352
ρ_{dl}	Dislocation density (m^{-2})	9×10^{13} [47]	5×10^{13} [57]
Z_i	Bias of interstitial-type defects for interstitials	1.05 [47]	1.05 [58]
η'	Cascade efficiency	0.2 [59]	0.1(MD)
$f_v(y)$	Clustering fraction of vacancy-type defect in cascade	Eq. (8.2) in [60]	MD
$f_i(p)$	Clustering fraction of interstitial-type defect in cascade	Eq. (8.1) in [60]	MD
$E_v^b(y)$	Binding energy of vacancy-typedefect (eV)	Eq. (6) in [61]	Table 4 in [62]
$E_i^b(p)$	Binding energy of interstitial-type defect (eV)	Eq. (1) in [63]	Table 4 in [62]
$E_v^m(1–4)$	Migration energy of vacancy-type defect (eV)	[64]	Table 3 in [62]
$E_i^m(1–4)$	Migration energy of interstitial-type defect (eV)	[64]	Table 3 in [62]

subsequently discretizing the resulting expressions, this method enables efficient grouping of large defect clusters ($y > N$) into size bins. In this work, we set $N = 200$ based on convergence tests demonstrating that increasing the number of discrete equations beyond this threshold yields negligible differences. When helium is present, it combines with vacancy-type clusters to form binary complexes. The evolution of these complexes is simulated using the combined 2D/1D domain approach proposed by Brimbal *et al.* [56].

B. Ion irradiation experiment

Irradiation experiments were conducted using the 1.7 MV tandem accelerator at Peking University. Iodine ions (I^{3+}) with an energy of 6.0 MeV were selected as incident particles, owing to their tunable beam intensities and minimal matrix disturbance [65]. The irradiation damage distribution was calculated using SRIM, as shown in Fig. 8 in Appendix A. To avoid interference from surface effects and implanted ions, the analyzed region was consistently defined as the subsurface layer spanning 200–400 nm beneath the irradiated surface. While iodine ions constitute foreign impurities in pure Ni, their low accumulated concentrations within this depth range ensure negligible influence on the measured radiation effects.

Cross-sectional specimens for TEM analysis were prepared via focused ion beam (FIB) milling, with specimen thickness determined by electron energy loss spectrometry (EELS); cavities were characterized using under-focused bright-field (BF) imaging, as detailed in our prior studies [66].

III. RESULTS

A. Overview of the approach

This work follows a multiscale but intentionally reduced workflow. The role of the CD simulations is to identify the controlling physical mechanisms and to test the consistency of the approximations that enable an analytical prediction framework. In particular, the simulations provide physical support for the mean-size approximation (MSA) and demonstrate that higher dose rates promote the nucleation of irradiation-induced sinks. Guided by these CD-based insights, we simplify the full rate-equation system using the MSA and derive a relationship linking cavity swelling to irradiation dose and dose rate at a fixed temperature. The resulting expression contains only a small number of parameters and is subsequently validated against experimental swelling data across different alloys, irradiation particles, doses, and dose rates. Finally, the framework is used as a predictive tool: high-dose-rate ion-irradiation data are used to determine the model parameters and to predict swelling under low-dose-rate neutron irradiation at the same temperature.

The central physical mechanism underlying this workflow is the dose-rate dependence of irradiation-induced defect nucleation. Under higher dose-rate conditions, more defects are generated per unit time, leading to a higher concentration of mobile defect clusters. This increases the frequency of cluster–cluster and cluster–sink interactions and promotes the nucleation of irradiation-induced defects, such as cavities and dislocation loops, as consistently observed in experiments [67–71] and mesoscale simulations [47,72]. Figure 1 schematically illustrates this

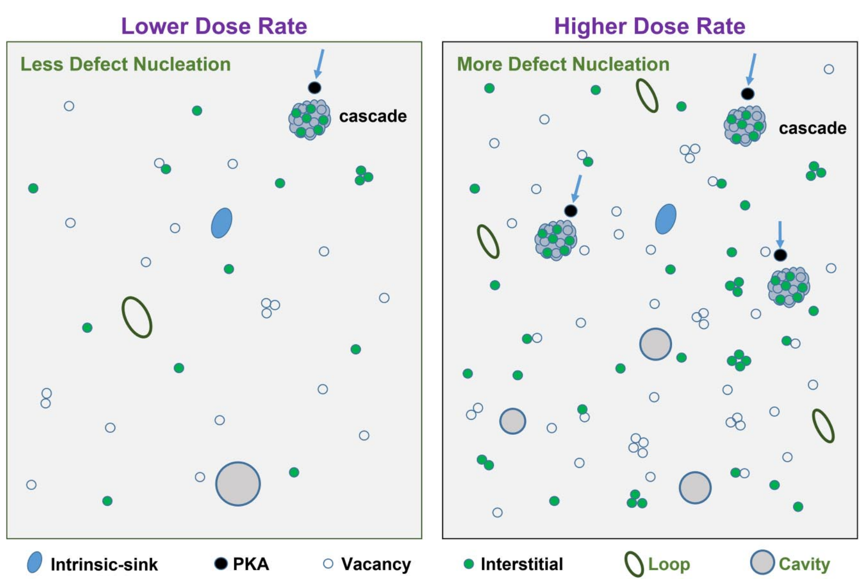

FIG. 1. Schematic illustration of the dose rate effects in materials. At higher dose rates, PKAs generate defects more rapidly through displacement cascades, which leads to a higher density of irradiation-induced defects, such as cavities and dislocation loops.

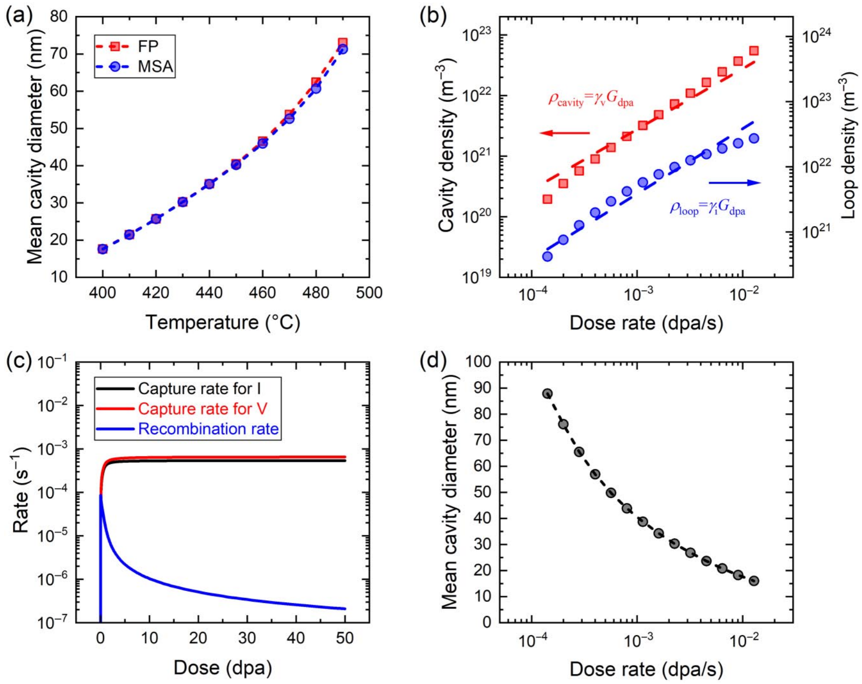

FIG. 2. CD simulation results underpinning the derivation of the quantitative relationship. (a) Comparison between the cavity diameter produced by the FP method and the MSA. (b) Dose-rate dependence of irradiation-induced cavity and dislocation loop densities. (c) Comparison between the recombination rate of displacement point defects and the capture rates of displacement point defects by sinks. (d) Dose-rate dependence of cavity size. Unless otherwise indicated, simulations are performed at 50 dpa, 450°C, and 1×10^{-3} dpa/s in BCC iron, with all non-varied parameters fixed at these values.

mechanism, highlighting the higher densities of irradiation-induced defects under higher dose-rate conditions. Within the CD framework, this qualitative picture can be described quantitatively.

B. Derivation of the quantitative relationship

This section establishes an analytical relationship linking volume swelling to both irradiation dose and dose rate, derived from a rational simplification of CD rate equations and supported by simulation evidence. Within the full CD framework, defects of each size are described by an independent concentration variable. The multiplicity of defect species introduces complexity into defect interaction kinetics. To derive analytical solutions, we first simplify the system by neglecting the size distribution of defects. For large defects produced during irradiation, the grouping scheme is generally utilized in CD simulations [47,49,73, 74]. The FP method provides detailed information on the size distribution of defect clusters, while the MSA, as the simplest grouping approach, treats TEM-visible defect clusters containing more than 50 constituent point defects as a single category, thereby ignoring their size distribution. Small cavities, which are not visible under TEM, exhibit a high thermal vacancy emission rate, while this rate is significantly reduced when they are stabilized by helium atoms produced from neutron transmutation reactions. In contrast, for the large cavities in the MSA size regime, the emission of vacancies can be neglected due to the high binding energies, irrespective of helium association, as shown in Fig. 9 in Appendix B. Figure 2(a) compares the cavity diameters obtained from the FP method and MSA, showing minimal deviation. The corresponding cavity densities are shown in Fig. 10(a) in Appendix B, and the same diameter data are included in Fig. 10(b) for completeness. Therefore, the MSA is applied to simplify the rate equations of TEM-visible defects. While results from both methods are similar, the FP method is employed as the default in subsequent CD simulations for improved precision.

Both experimental and computational studies demonstrate that irradiation-induced cavity and dislocation loop densities initially rise rapidly with dose before saturating at low doses [48,68,75–78]—a trend replicated in CD simulations, as shown in Fig. 11 in Appendix B. Consequently, these densities are approximated as time-independent constants during cavity growth. While mobile clusters interact with multiple sinks, TEM-visible defects dominate the total irradiation-induced sink strength, as shown in Fig. 12 in Appendix B, allowing mobile clusters to be considered as interacting primarily with TEM-visible sinks. Figure 13 in Appendix B shows that the defect flux responsible for cavity growth in the MSA size regime is dominated by single vacancies and self-interstitials. Therefore, it is sufficient to retain only point defects in the rate equations used to describe cavity growth. Within the framework of MSA and building upon the above approximations, the rate equations of interstitials and vacancies are simplified as:

$$\frac{\mathrm{d}C_\mathrm{i}}{\mathrm{d}t} = G_\mathrm{i} - K_\mathrm{iv}C_\mathrm{i}C_\mathrm{v} - D_\mathrm{i}C_\mathrm{i} \times \left(S_\mathrm{i0} + \frac{\pi}{\Omega}Z_\mathrm{i}R_\mathrm{loop}\rho_\mathrm{loop} + \frac{4\pi}{\Omega}R_\mathrm{cavity}\rho_\mathrm{cavity}\right) \quad (1)$$

$$\frac{\mathrm{d}C_\mathrm{v}}{\mathrm{d}t} = G_\mathrm{v} - K_\mathrm{iv}C_\mathrm{i}C_\mathrm{v} - D_\mathrm{v}C_\mathrm{v} \times \left(S_\mathrm{v0} + \frac{\pi}{\Omega}Z_\mathrm{v}R_\mathrm{loop}\rho_\mathrm{loop} + \frac{4\pi}{\Omega}R_\mathrm{cavity}\rho_\mathrm{cavity}\right). \quad (2)$$

In the above equations, C_i and C_v are the concentrations of interstitials and vacancies, respectively. G_i and G_v are the production rates of point defects from cascades. R_loop and R_cavity are the radii of the interstitial-type defect and the vacancy-type defect in the MSA size regime, respectively. D_i and D_v are the diffusion coefficients.

The density of irradiation-induced defects has been experimentally observed to increase with the dose rate [67–70]. This trend is quantitatively captured by CD simulations, which reveal that the defect densities (ρ_cavity for cavity and ρ_loop for dislocation loop) exhibit an approximately linear dependence on the dose rate, as illustrated in Fig. 2(b). Results at different temperatures are further shown in Fig. 14 in Appendix B. To derive a practically usable analytical expression, this dose-rate dependence is represented by a linear approximation rather than by a strict fit to the full CD simulation data:

$$\rho_\mathrm{loop} \cong \gamma_\mathrm{i}G_\mathrm{dpa}, \qquad \rho_\mathrm{cavity} \cong \gamma_\mathrm{v}G_\mathrm{dpa}, \quad (3)$$

where G_dpa is the dose rate, γ is a proportionality constant representing the irradiation-induced defect nucleation capability at a specific temperature.

Herein, we classify the defect sinks in the irradiated alloys into two types: intrinsic sinks, with sink strength for vacancies and interstitials denoted as S_v0 and S_i0, respectively, and irradiation-induced sinks, with sink strength for vacancies and interstitials denoted as S'_v and S'_i, respectively. CD simulations demonstrate that the concentrations of vacancies and interstitials rapidly reach quasi-steady states [48,56] enabling time-independent approximations for MSA-size-regime sink strengths. Crucially, dose rate variations predominantly alter defect densities (ρ_cavity, ρ_loop) rather than cluster sizes (R_cavity, R_loop), establishing defect density as the dominant factor in sink strength evolution. As can be seen from Fig. 15 of Appendix B, the sink strength also exhibits an approximately linear dependence on the dose rate. These insights permit further simplification of the rate equations governing defect interactions. Using the approximate dose-rate dependence of the irradiation-induced defect densities in Eq. (3), the irradiation-induced sink strengths for interstitials and vacancies can be written as

$$S'_\mathrm{i}(G_\mathrm{dpa}) = \frac{\pi}{\Omega}Z_\mathrm{i}R_\mathrm{loop}\gamma_\mathrm{i}G_\mathrm{dpa} + \frac{4\pi}{\Omega}R_\mathrm{cavity}\gamma_\mathrm{v}G_\mathrm{dpa} = \delta_\mathrm{i}G_\mathrm{dpa}, \quad (4)$$

$$S'_\mathrm{v}(G_\mathrm{dpa}) = \frac{\pi}{\Omega}Z_\mathrm{v}R_\mathrm{loop}\gamma_\mathrm{i}G_\mathrm{dpa} + \frac{4\pi}{\Omega}R_\mathrm{cavity}\gamma_\mathrm{v}G_\mathrm{dpa} = \delta_\mathrm{v}G_\mathrm{dpa}. \quad (5)$$

Here, $\delta_\mathrm{i}$and δ_v are proportionality coefficients that convert the dose-rate-enhanced irradiation-induced defect densities into the corresponding sink strengths for interstitials and vacancies, respectively. The parameters R_cavity and R_loop can be regarded as coefficients applied to transform the densities of irradiation-induced defects into their sink strengths for interstitials and vacancies. Since the changes in sink strength of irradiation-induced defects are primarily governed by variations in their densities under different dose rates, the overall sink strengths of vacancies and interstitials can be approximately expressed as $S_\mathrm{v} = S_\mathrm{v0} + S'_\mathrm{v} = S_\mathrm{v0} + \delta_\mathrm{v}G_\mathrm{dpa}$ and $S_\mathrm{i} = S_\mathrm{i0} + S'_\mathrm{i} = S_\mathrm{i0} + \delta_\mathrm{i}G_\mathrm{dpa}$.

CD simulations reveal that at high doses, irradiation-induced defect sinks exhibit significantly higher capture rates for interstitials and vacancies than their mutual recombination rates, as shown in Fig. 2(c). The complete results are given in Fig. 16 in Appendix B. Therefore, the dominant-sink-capture condition can be expressed as

$$K_\mathrm{iv}C_\mathrm{i}C_\mathrm{v} \ll D_\mathrm{i}S_\mathrm{i}C_\mathrm{i}, \quad (6)$$

$$K_\mathrm{iv}C_\mathrm{i}C_\mathrm{v} \ll D_\mathrm{v}S_\mathrm{v}C_\mathrm{v}. \quad (7)$$

Under this condition, the recombination term can be neglected in the quasi-steady-state solutions for the point-defect concentrations. The quasi-steady-state solutions to the concentrations of interstitials and vacancies are determined as

$$C_\mathrm{i} = \frac{G_\mathrm{i}}{D_\mathrm{i}[S_\mathrm{i0} + S'_\mathrm{i}(G_\mathrm{dpa})]}, \quad (8)$$

$$C_\mathrm{v} = \frac{G_\mathrm{v}}{D_\mathrm{v}[S_\mathrm{v0} + S'_\mathrm{v}(G_\mathrm{dpa})]}. \quad (9)$$

Within the MSA framework, the growth equation for TEM-visible cavities can be expressed as:

$$\frac{\mathrm{d}R_{\mathrm{cavity}}}{\mathrm{d}t} = \frac{1}{R_{\mathrm{cavity}}}[D_{\mathrm{v}}C_{\mathrm{v}} - D_{\mathrm{i}}C_{\mathrm{i}}]. \tag{10}$$

Substituting the concentrations of interstitials and vacancies into Eq. (10), the growth equation of cavities is simplified as

$$\frac{\mathrm{d}R_{\mathrm{cavity}}}{\mathrm{d}t} = \frac{1}{R_{\mathrm{cavity}}}\left[\frac{G_{\mathrm{v}}}{S_{\mathrm{v0}} + S'_{\mathrm{v}}(G_{\mathrm{dpa}})} - \frac{G_{\mathrm{i}}}{S_{\mathrm{i0}} + S'_{\mathrm{i}}(G_{\mathrm{dpa}})}\right]. \tag{11}$$

It should be emphasized that the above growth equation is valid after the incubation period, characterized by the incubation dose Δ_0. Therefore, the initial condition for the above growth equation is found to be:

$$R_{\mathrm{cavity}}\left(\frac{\Delta_0}{G_{\mathrm{dpa}}}\right) \cong 0. \tag{12}$$

Substituting Eqs. (4) and (5) into the solution of Eq. (11), the mean radius of cavities is solved as

$$R_{\mathrm{cavity}} = \left[\frac{2(\eta_{\mathrm{v}} - \frac{\eta_{\mathrm{i}}}{b})}{S_{\mathrm{v0}}}\frac{1}{1 + \frac{\delta_v}{S_{\mathrm{v0}}}G_{\mathrm{dpa}}}\right]^{1/2}(\Delta_{\mathrm{dpa}} - \Delta_0)^{1/2}, \tag{13}$$

where $\eta_{\mathrm{v}} = \frac{G_{\mathrm{v}}}{G_{\mathrm{dpa}}}, \eta_{\mathrm{i}} = \frac{G_{\mathrm{i}}}{G_{\mathrm{dpa}}}$, η_{v} and η_{i} represent the cascade efficiency ratios for vacancies and interstitials surviving athermal annealing, respectively. In the full CD simulations, the total numbers of vacancies and self-interstitials produced in cascades are identical. However, the cascade-produced defects are partitioned into isolated point defects and vacancy-/interstitial-type clusters. Therefore, the source efficiencies of freely migrating single vacancies and self-interstitials in the reduced description, denoted by η_{v} and η_{i}, are retained separately to reflect cascade damage partitioning under ion and neutron irradiation. This notation does not imply that continued cavity growth is dominated by production bias. Indeed, flux analysis in the full CD simulations shows that, during the cavity-growth stage, the ratio of vacancy flux to interstitial flux absorbed by growing cavities is above unity and remains below the prescribed interstitial-sink bias. Thus, the net vacancy flux required for cavity growth is mainly generated by sink bias. The parameter b is the total bias factor, defined as $b = S_{\mathrm{i}}/S_{\mathrm{v}}$. A key mechanism is that increased dose rates enhance irradiation-induced sinks, leading to a reduction in cavity size. Although multiple approximations were made in the derivation, CD simulations confirm that cavity size decreases with increasing dose rate in Fig. 2(d), and the same trend remains valid for Fe–9Cr, Ni, and cases with different intrinsic dislocation densities, as shown in Fig. 17 in Appendix B.

From the definition of cavity swelling, Swelling $= \rho_{\mathrm{cavity}}\frac{4}{3}\pi R_{\mathrm{cavity}}{}^3$, and using the approximate relation in Eq. (3), the swelling can be expressed in terms of dose and dose rate. Introducing an effective dose-rate-dependent swelling coefficient α, which collects the prefactors associated with irradiation-induced cavity density and cavity-growth kinetics, the swelling relationship is obtained as:

$$\mathrm{Swelling}(G_{\mathrm{dpa}}, \Delta_{\mathrm{dpa}}) = \alpha(\Delta_{\mathrm{dpa}} - \Delta_0)^{3/2}. \tag{14}$$

The coefficient α is given by

$$\alpha = \alpha'\frac{G_{\mathrm{dpa}}}{(1 + kG_{\mathrm{dpa}})^{3/2}},$$

$$\alpha' = \frac{4}{3}\pi\gamma_{\mathrm{v}}\left[\frac{2(\eta_{\mathrm{v}} - \frac{\eta_{\mathrm{i}}}{b})}{S_{\mathrm{v0}}}\right]^{3/2},$$

$$k = \frac{\delta_{\mathrm{v}}}{S_{\mathrm{v0}}}. \tag{15}$$

Through CD simulations, W. G. Wolfer *et al.* revealed that the incubation dose Δ_0, which roughly marks the transition to steady-state swelling and is strongly dependent on both irradiation temperature and dose rate, is closely related to and even controlled by the evolution of the dislocation structure [72]. Their theoretical predictions show excellent agreement with the systematic experimental results reported by F. A. Garner *et al.* [35]. Physically, Δ_0 should be regarded as an effective incubation dose governed by the combined competition among cavity nucleation, dislocation-loop evolution, intrinsic sinks, and the redistribution of vacancy and interstitial fluxes between cavities and dislocation networks during irradiation. In this work, the parameter d is introduced to quantify the influence of dose rate on this competition for a given material at a specific temperature. Following the work of F. A. Garner *et al.* [35], we express the incubation dose as:

$$\Delta_0 = c + d\,\mathrm{lg}(G_{\mathrm{dpa}}). \tag{16}$$

Parameters c and d are material parameters independent of dose rate.

The cavity growth equations derived above result from a rational simplification of the CD rate equations, guided by empirical trends observed in simulations. This approach was intentionally adopted instead of directly applying conventional rate theory, which typically relies on numerous a priori assumptions. By grounding the simplifications in simulation-based evidence, the present formulation minimizes the introduction of unverified assumptions while retaining the essential physics governing irradiation-induced swelling.

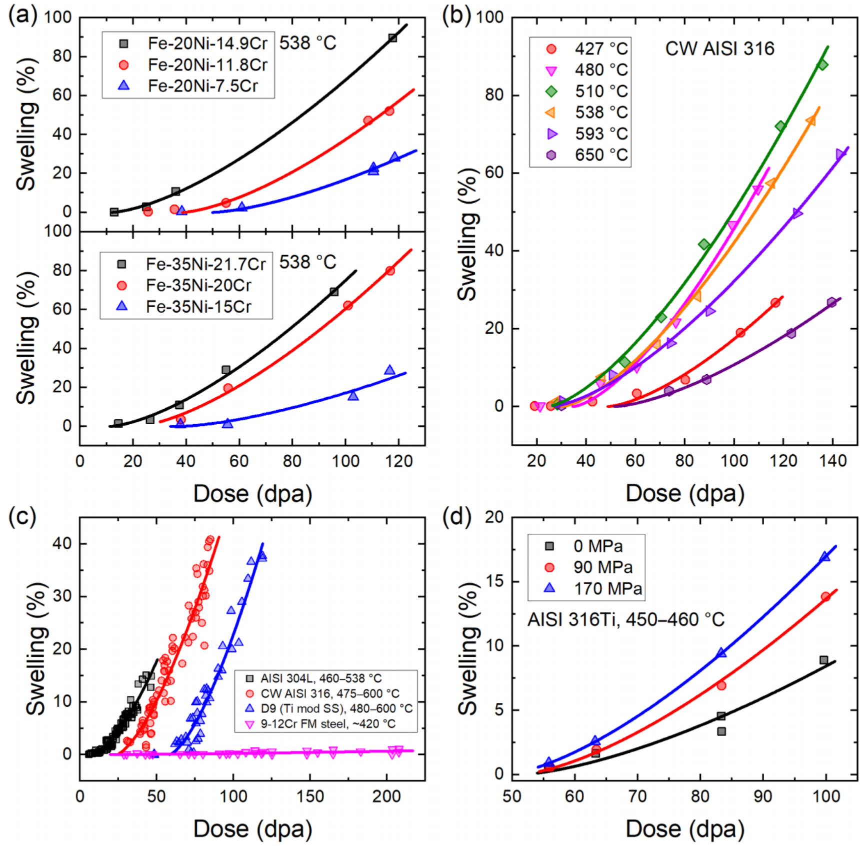

FIG. 3. Validation of the derived quantitative relationship using available irradiation data in different alloys and under various conditions, where each curve is fitted with its own values of α and Δ_0. (a) Fe-20Ni-xCr and Fe-35Ni-xCr irradiated by neutrons at 538°C [32]. (b) Cold-worked AISI 316 stainless steel irradiated by neutrons at different temperatures [32]. (c) Annealed AISI 304L, cold-worked AISI 316, and D9 austenitic stainless steel and 9%–12% Cr tempered ferritic/martensitic steel irradiated by neutrons [4,32,33]. (d) AISI 316Ti irradiated by neutrons at different pressures [34].

C. Swelling induced by energetic heavy-ion and neutron irradiations

This section demonstrates that the derived relationship consistently captures the dose dependence of swelling across different alloys and irradiation conditions and quantitatively describes its systematic variation with dose rate using a single set of material-specific parameters. These formulas provide the quantitative dependence of volume swelling on different parameters at a fixed temperature, including model parameters (α', k, c, d), as well as the irradiation variables: irradiation dose (Δ_{dpa}) and dose rate (G_{dpa}). The parameter α' and k are complicated functions of material characteristics (including intrinsic sink strengths, defect diffusion barriers, and so on) and temperature. The incubation Δ_0 is governed by the capability of cavities to be nucleated, expected as a complicated function of materials' characteristics and irradiation parameters (including dose rate and temperature).

Equation (14) predicts a nonlinear relation between cavity swelling and irradiation dose. When dose rate effects are not considered, α is constant, and the values of α' and k cannot be determined. Figure 3 shows the good fitting of experimental irradiation data to Eq. (14) for different conditions, including varying materials, temperatures, and pressure [4,32,33,34]. The successful fitting with parameters α and Δ_0—both of which are independent of the irradiation dose—demonstrates that the parameter separation in the relationship is effective. Moreover, the consistent 1.5-power dependence observed under all investigated conditions confirms that the proposed relationship provides a robust description of the dose dependence of cavity swelling in structural alloys (a more thorough validation is provided in Appendix C). Dependence observed under all investigated conditions confirms that the proposed relationship provides a robust description of the dose dependence of cavity swelling in structural alloys (a more thorough validation is provided in Appendix C).

Figure 4 demonstrates that a single set of fixed parameters (α', k, c, and d) in Eqs. (14)–(16) successfully describes the cavity swelling of a given material at a fixed temperature across a range of dose rates [11,17,35,36]. This formulation originates from recognizing that while the parameter α in Eq. (14) is independent of dose, it inherently depends on dose rate; therefore, α is separated

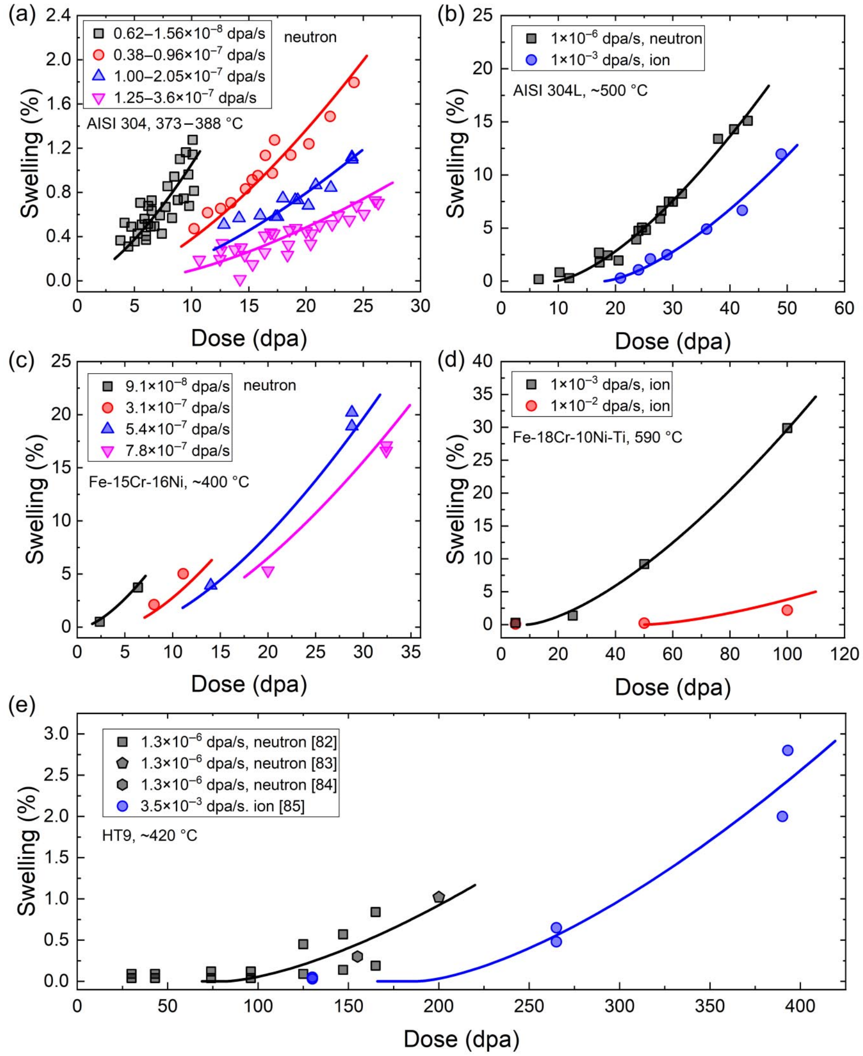

FIG. 4. Validation of the proposed quantitative relationship using available irradiation data with different dose rates for the same alloy (α', k, c, and d hold constant for a given alloy). (a) AISI 304 irradiated with different dose-rate neutrons [11], (b) AISI 304L irradiated by neutrons and 3.5 MeV Fe^{+} [36], (c) Fe-15Cr-16Ni irradiated with different dose-rate neutrons [17], (d) Fe-18Cr-10Ni-Ti irradiated with different dose-rate 2 MeV Cr^{+} [35], and (e) HT9 irradiated by neutrons in FFTF [79–81] and 3.5 MeV Fe^{+} [82]. The solid lines are our fitting results.

into a dose-rate-independent part α' and a dose-rate function, $\frac{G_{\mathrm{dpa}}}{(1+kG_{\mathrm{dpa}})^{3/2}}$, with α' and k being intrinsic material parameters unaffected by dose rate. The successful fitting in Fig. 4 confirms that this parameter separation is effective. Importantly, the validation in Fig. 4 covers the major classes of structural alloys for which systematic swelling data at different dose rates are available, including *fcc* austenitic stainless steels and *bcc* ferritic/martensitic steels, demonstrating the general applicability of the proposed dose-and-dose-rate relationship to structural materials. Notably, Fig. 4(b) and 4(e) further shows that the data from both ion- and neutron-irradiation can be captured by the same formulation. The fitting results shown in Figs. 3 and 4 demonstrate that the established relationship well captures the dependence of cavity swelling on both irradiation dose and dose rate for different complex alloys under neutron and heavy-ion irradiation conditions, within the same elevated temperature in the normal experimental temperature range.

The capture of the dose dependence of swelling, shown in Fig. 3, makes it possible to predict swelling at high doses based on low-dose irradiation data. In addition, the fitting results in Fig. 4 indicate the quantitative correlation of the swelling with irradiation dose at different dose rates (G_{dpa}), or with different energetic particles, making the equivalence possible between different energetic particles, especially between heavy-ion and neutron irradiations in terms of volume swelling in the same material at the same elevated temperatures.

D. Prediction method of volume swelling

Building on the validated relationship, this section demonstrates that (i) volume swelling at high irradiation doses can be quantitatively predicted from low-dose data at a given dose rate and (ii) swelling at one dose rate can be extrapolated from data obtained at a different dose rate, enabling predictions beyond experimentally accessible regimes. This capability is particularly important for rapid screening and evaluation of structural materials, given that acquiring high-dose neutron irradiation data typically requires many years of irradiation and PIE. In Fig. 5(a), the parameters α and Δ_0 are calculated using irradiation data from the dose range of 40–70 dpa [37] (parameter values are provided in Appendix E). Using these parameters, Eq. (14) is then applied to predict the swelling behavior in the 70–85 dpa range. The predicted swelling shows excellent agreement with the practical experimental data, validating the dose-extrapolation capability of our approach.

Irradiation at different dose rates results in different swelling levels at the same dose under the same temperature. The concept of equivalent dose is introduced to achieve identical swelling at different dose rates by adjusting the irradiation dose under the same temperature. Based on Eqs. (14)–(16), the equivalent dose can be derived as follows:

$$\Delta_{\mathrm{dpa2}} = \frac{1 + kG_{\mathrm{dpa2}}}{1 + kG_{\mathrm{dpa1}}}\left(\frac{G_{\mathrm{dpa1}}}{G_{\mathrm{dpa2}}}\right)^{\frac{2}{3}} \times [\Delta_{\mathrm{dpa1}} - \Delta_0(G_{\mathrm{dpa1}})] + \Delta_0(G_{\mathrm{dpa2}}). \quad (17)$$

To reach a specific swelling level, a dose of Δ_{dpa1} is required at a dose rate G_{dpa1}, while an equivalent dose Δ_{dpa2} is needed at a different dose rate G_{dpa2} to achieve the same swelling level under the same temperature. By fitting the available experimental data, the values of k and parameters c and d for the same alloys can be determined. This equation serves as the basis for predicting the swelling level for an identical alloy at the same or similar elevated temperature at given irradiation conditions. Figure 5(b) illustrates the derivation of the equivalent dose corresponding to the same swelling level. In Fig. 5(b), the parameters k, c, and d for CW AISI 316 are determined from two sets of irradiation data at different dose rates (black symbols) [37,38], where neutron-irradiation data below 50 dpa and ion-irradiation data are used for fitting, while the high-dose neutron data are reserved for validation. Based on these fitted parameters, the irradiation dose required to produce the same swelling at 5×10^{-7} dpa/s can be deduced from the data at 1.74×10^{-3} dpa/s. Although the low-dose neutron data exhibit substantial scatter, the equivalent-dose points calculated from the ion-irradiation data lie within the range of the high-dose neutron measurements. Therefore, these examples suggest that our derived relationship is capable of predicting volume swelling at high doses from the low dose data, correlating the irradiation dose with different given dose rates, and predicting the equivalent dose for low-dose-rate irradiation from high-dose-rate experiments.

E. Experimental validation of prediction method: From ion irradiation to neutron irradiation

This section provides a stringent experimental validation of the proposed framework by demonstrating that neutron-irradiation-induced swelling can be quantitatively predicted using ion-irradiation data alone, despite dose-rate differences spanning approximately four orders of magnitude. In the preceding analysis, the concept of an equivalent dose was shown to enable prediction of high-dose neutron swelling from ion-irradiation data when supplemented by limited low-dose neutron irradiation data in the parameter fitting. While this represents an important

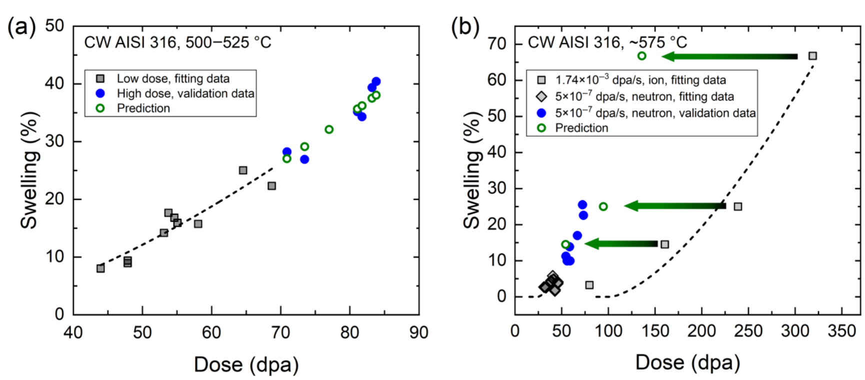

FIG. 5. Quantitative prediction of swelling level. (a) Prediction of swelling in CW AISI 316 from low to high doses. The parameters are calculated using the first 60% of the low-dose neutron irradiation data (black symbols), while the remaining neutron data are reserved for validation [37]. (b) Prediction of swelling in CW AISI 316 at a low dose rate (5×10^{-7} dpa/s) using data obtained at a high dose rate (1.74×10^{-3} dpa/s) at the same swelling level. The parameters are calculated from the low-dose neutron irradiation and ion irradiation data (black symbols) [37,38].

step toward correlating ion and neutron irradiation, it does not address a more fundamental and long-standing challenge in the field: whether neutron-irradiation-induced swelling can be predicted without recourse to any neutron data, relying exclusively on ion-irradiation experiments conducted at much higher dose rates. To assess the potential of our approach in addressing this fundamental challenge, ion irradiation experiments must be performed at different dose rates and doses.

To eliminate confounding factors arising from material variations (e.g., composition differences and manufacturing processes), we selected pure metals to establish and validate the prediction method. This ensures identical material properties between ion- and neutron-irradiated specimens. Considering that FCC metals exhibit more pronounced swelling compared to BCC metals, pure Ni was chosen as the model material. Pure Ni specimens were irradiated by 6 MeV I^{3+} ions at 450°C. The irradiation conditions and the mean swelling and the corresponding standard deviation are listed in Table II, and the specific experimental procedures are discussed in the Methods section.

The parameters can be determined by fitting the experimental data listed in Table II. Because of the inherent uncertainties in repeated TEM observations, a Monte Carlo method was employed to evaluate the associated errors [83,84]. The detailed procedure and the fitted parameters are provided in Appendix E. Using these parameters, Eqs. (14)–(16) were applied to predict swelling under neutron-irradiation conditions at 450°C, as reported by Budylkin *et al.* [85]. While neutron irradiation inevitably produces transmutation gases, our prior ion irradiation experiments [66] on pure Ni at 450°C indicate that their influence on swelling is relatively minor. Based on the work of Ayanoglu *et al.* [27], the helium generation rate for pure nickel in the BOR-60 fast reactor is estimated to be 3 appm He/dpa. CD simulations under corresponding neutron irradiation conditions reveal that while helium enhances cavity nucleation, the resultant increase in swelling is only 23% compared to the helium-free case, as detailed in Fig. 20 in Appendix D. This result provides further support for the conclusion drawn from our prior ion irradiation experiments, confirming the secondary role of helium in swelling compared to the dose rate effect.

TABLE II. Ion irradiation conditions and swelling results for pure Ni under 6 MeV I^{3+} ion bombardment at 450°C.

Dose (dpa)	Dose rate (dpa/s)	Swelling (%)
5.5	2.0×10^{-3}	0.109 ± 0.046
5.5	6.5×10^{-3}	0.047 ± 0.009
5.5	1.2×10^{-2}	0.031 ± 0.011
16.4	6.5×10^{-3}	0.197 ± 0.022
16.4	1.2×10^{-2}	0.099 ± 0.017

TABLE III. Neutron irradiation conditions and swelling results for pure Ni at 450°C in BOR-60 fast reactor [85] and predictions.

Dose (dpa)	Dose rate (dpa/s)	Swelling (%)	Prediction (%)
38	3.7×10^{-7}	3.9	6.2 ± 1.3
51	3.3×10^{-7}	6.0	8.4 ± 1.8

Therefore, in the present analysis, only displacement damage is considered.

The neutron irradiation conditions and swelling results from the literature, along with the predictions, are summarized in Table III. The data from Tables II and III are plotted in Fig. 6(a) for direct comparison. Despite the four-order-of-magnitude difference in dose rate and the two-order-of-magnitude variation in swelling, the predicted neutron swelling values are within a factor of two of the experimental measurements. This agreement demonstrates that the proposed dose-and-dose-rate relationship can predict neutron-induced swelling using ion-irradiation data obtained at the same temperature. A comparison with the traditional invariance-theory-based temperature-shift approach is provided in Appendix F.

The stark contrast between our model's accuracy and the classical theory's massive deviation demonstrates that our approach can reliably predict neutron-induced swelling based on ion-irradiation data. This capability is particularly significant for accelerating the development of radiation-resistant materials, as it provides a robust, physically grounded way to predict long-term neutron effects through rapid and cost-effective ion irradiation experiments.

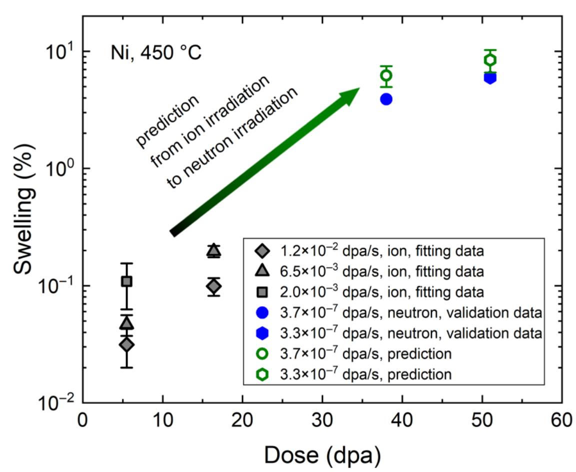

FIG. 6. Prediction of neutron-induced swelling in pure Ni at 450°C. The model parameters are determined using ion-irradiation data obtained at different dose rates at 450°C and are then used to predict swelling under neutron-irradiation conditions at the same temperature. The neutron-irradiation data are taken from Ref. [85].

F. Swelling resistance of different materials

The preceding results demonstrate that the formulas developed in this study can reliably describe the swelling response of different materials under irradiation. Nevertheless, a key remaining question is how to compare the irradiation resistance among these materials. Irradiation effects in materials are complex processes, including defect production and evolution. Previous works have established that volume swelling can be influenced by different properties of materials, e.g., compositions and their atomic weights, crystal structures, grain boundaries and interfaces, atomic bonds, solute segregation and precipitation, the diffusivity of defects, and sink strength. [17,86]. To establish a unified description of irradiation swelling behavior across different materials, we use the simple parameter ratio of Δ_0/α as an index to characterize the relative swelling resistance of materials under neutron irradiation at similar dose rates. The overall swelling of materials relies on both Δ_0 and α since the dose-dependent swelling includes an initial nucleation/incubation period, followed by a growth stage [87,88]. A material with enhanced swelling resistance would have a high Δ_0 but a low α so that there are a prolonged incubation period and a low growth rate. With this definition, higher values of Δ_0/α correspond to better swelling resistance in a material.

A summary of Δ_0/α values for different materials under neutron irradiation is demonstrated in Fig. 7, together with the temperature at which Δ_0/α is obtained. Among all the materials, Cu exhibits the lowest Δ_0/α due to its poor swelling resistance. On the other hand, MA957, a type of oxide dispersion strengthened (ODS) steel, possesses the highest Δ_0/α among the materials examined, suggesting that its excellent ability to suppress swelling is due to the high density of nanoparticles that provide numerous defect sinks to absorb the mobile vacancies. For the same material AISI 316, the curve of Δ_0/α with the temperature at

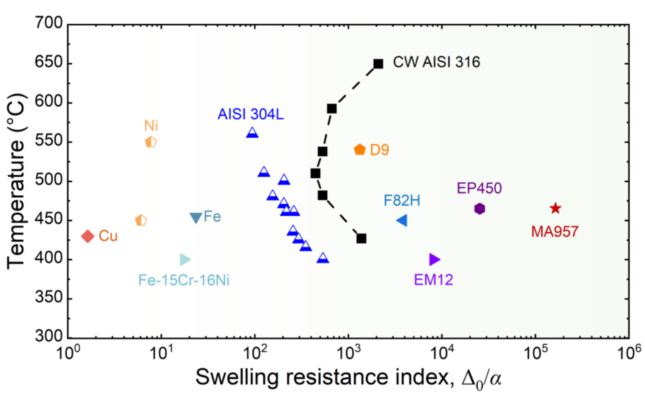

FIG. 7. Swelling resistance (characterized by Δ_0/α) of different materials at different working temperatures under neutron irradiation [4,17,33,36,32,91–94]. The irradiation dose rates are similar.

reactor-relevant dose rates is in accordance with the experimental swelling peak at about 510°C. Note that Δ_0/α also depends on the dose rate, and the comparison in Fig. 7 is made at similar dose rates.

IV. DISCUSSION

While computational methods such as CD and OKMC simulations have provided profound mechanistic insights into irradiation damage evolution, their predictive power for engineering alloys is often constrained by two intrinsic challenges. First, they require a large set of physical parameters—many of which are difficult to measure or calculate accurately beyond pure metals or simple model systems. Even for pure metals, reliable parameters may be challenging to obtain. In tungsten, for example, conventional DFT predicts repulsive divacancies, yet experiments observe vacancy clustering into voids—a contradiction resolved only by accounting for entropic effects at finite temperature [89]. Second, and more critically, explicitly modeling the complex, heterogeneous microstructure of real alloys (e.g., precipitates, grain boundaries, and dislocation networks) within these computational frameworks remains a formidable problem.

A widely used route for bridging ion and neutron swelling is the temperature-shift concept rooted in invariance theory. This framework is fundamentally derived for steady-state swelling conditions [90], whereas swelling evolution over the full dose range is intrinsically nonlinear, progressing through incubation, transient growth, and steady-state regimes. As a result, even when a temperature shift can be defined for steady-state rates, it does not directly quantify dose-dependent differences—particularly the incubation behavior that often dominates a material's swelling resistance, as illustrated in Fig. 7. Moreover, although in principle the temperature shift can be expressed in terms of defect energetics and kinetic regimes [90], in engineering alloys these regime assignments and the relevant defect energetics are often uncertain. Notably, even for pure metals, the predicted shift can vary substantially when alternative recommended values of key transport mobilities are used, resulting in an uncertainty on the order of ~50 °C [90]. In steels, the situation is further complicated by impurity–vacancy interactions: solute atoms can drag moving vacancies, markedly reducing vacancy mobility, yielding an effective vacancy migration barrier as high as ~1.37 eV [48], whereas previous temperature-shift analyses have sometimes employed the pure-Fe value (~0.62 eV) when estimating shifts for steels [24].

In contrast, the approach developed here provides an alternative route by integrating the qualitative physical principles revealed by such simulations with quantitative experimental data, thereby yielding an explicit dose-and-dose-rate relationship at fixed temperature and capturing the full dose-dependent evolution of swelling.

Accordingly, the duration of the incubation period is quantified directly within our formulation rather than inferred indirectly from steady-state shifts. The key material-specific information is embedded in the experimentally measured swelling response under high-dose-rate ion irradiation. Consequently, our approach does not rely on explicitly defining every microscopic parameter; instead, it leverages the material's own behavior as the ultimate descriptor. This enables the derived relationship to be directly applicable across diverse materials and, most importantly, provides a validated pathway for extrapolating high-dose-rate results to predict long-term swelling under low-dose-rate neutron irradiation. More broadly, the success of the same functional form in describing swelling across multiple alloy classes suggests that the framework captures common kinetic features governing cavity swelling in structural materials. In this sense, the fitted parameters are not merely empirical constants for individual datasets, but compact descriptors of material response that can be used to compare swelling resistance across alloys, as illustrated by the swelling-resistance index in Fig. 7.

Our approach developed herein is application-oriented and is based on a simplified description of irradiation-induced volume swelling in alloys by simplifying the rate equations within the framework of CD and by simplifying the dose-rate-enhanced defect nucleation based on CD simulations. However, this description does not hold in all cases. For example, in deriving the cavity growth equations, thermal dissociation of TEM-visible cavities was neglected because, at typical irradiation temperatures, the thermal dissociation rate is negligible compared to irradiation-driven defect fluxes [47]. However, as temperature increases, the thermal dissociation rate rises exponentially, eventually becoming significant even for TEM-visible cavities. Therefore, neutron-induced swelling exhibits a temperature window [95–97]. At temperatures well above recovery stage V, irradiation tends to generate a high concentration of dispersed vacancies rather than stable cavities, making swelling unlikely to occur [97]. This high-temperature limit corresponds to the swelling cutoff temperature. Correspondingly, conditions near or beyond this cutoff may violate the assumptions of our model. Hence, it is beneficial to constrain the applicable temperature range of the approach for predicting neutron irradiation swelling. For the present purpose, this temperature range should be defined with respect to the target neutron dose rate. Since the peak swelling temperature increases with dose rate [35,95,96,98], the temperature range in which high-dose-rate ion irradiation produces significant swelling may be shifted above the corresponding neutron-irradiation swelling window. Therefore, a conservative criterion is to apply the present framework at temperatures around the peak swelling temperature corresponding to the neutron dose rate, provided that the condition remains within the swelling-active regime. Near the swelling cutoff temperature, decreasing the dose rate can make stable cavity nucleation increasingly difficult; for example, the CD simulations in Ref. [72] show that, at high temperatures, reducing the dose rate can cause the incubation dose to increase substantially or even become effectively very large. Under such conditions, observable cavity swelling may be absent, and the assumptions underlying the present reduced description may no longer be satisfied.

The present framework should be regarded as a swelling-focused description for materials and conditions where cavity swelling is experimentally observable. The diversity of materials, especially advanced alloys with complex intrinsic sinks (e.g., grain boundaries, precipitates, or dispersed nanoparticles), introduces additional variables that may significantly alter defect evolution dynamics [99]. However, in this study, the intrinsic sinks are not studied in depth, most of the literature data that can be used to validate the irradiation condition dependence are for pure metals and mature alloys. Meanwhile, some advanced alloys show excellent swelling resistance without observable cavities. How to establish a reasonable prediction method for such situation is still a challenge. Therefore, for advanced alloys where data are lacking or without swelling, the effectiveness of this approach requires further investigation.

V. CONCLUSIONS

By focusing on dose-rate-enhanced defect nucleation and leveraging CD and rate equations, we establish a relationship that describes volume swelling in alloys irradiated by different energetic particles over a wide range of dose rates at a given temperature. CD simulations and experimental results show that the densities of irradiation-induced defects increase with dose rate, owing to higher concentrations of mobile clusters that promote defect nucleation. This enhanced nucleation modifies cavity growth and leads to pronounced differences in swelling under different dose rates at the same accumulated dose.

The proposed relationship quantitatively captures the dependence of swelling on both irradiation dose and dose rate across diverse materials and irradiation conditions. Validation using extensive literature data and dedicated ion-irradiation experiments confirms that the framework enables reliable prediction of low-dose-rate swelling from high-dose-rate data, including extrapolation from heavy-ion to neutron irradiation.

Although CD simulations are restricted to model metals, the derived relationship successfully describes swelling behavior in multicomponent alloys, indicating that the underlying mechanisms of defect nucleation and growth revealed by CD remain operative in engineering materials. Based on this framework, the combined parameter Δ_0/α is proposed as a quantitative metric to compare the swelling resistance of structural alloys under reactor-relevant conditions.

Overall, this work provides a physically grounded and practical predictive framework for evaluating irradiation-induced swelling, offering a rapid screening approach for assessing the long-term performance of structural materials in advanced nuclear energy systems. Future work could explore its extension to predict other irradiation-sensitive properties, such as irradiation-induced hardening or irradiation-enhanced creep, provided the dominant microstructural features governing those properties are identified and incorporated.

ACKNOWLEDGMENTS

This work is supported by the National Natural Science Foundation of China (Grant Nos. 12192280, 12422514, 11935004, and 12275009) and the National MCF Energy R&D Program 2022YFE03110000. The authors gratefully acknowledge the computing resources and support provided by the High Performance Computing Platform of the Center for Life Science (Peking University).

DATA AVAILABILITY

The data from the literature used in this study are identified by the corresponding cited references. The main data generated in this work are provided in the tables within the article.

APPENDIX A: SRIM CALCULATION

The irradiation damage distribution and implanted ion concentrations were calculated via SRIM simulations, as shown in Fig. 8. The quick Kinchin-Pease mode was adopted, and the displacement threshold energy and the lattice binding energy were set to 40 and 0 eV, respectively [100].

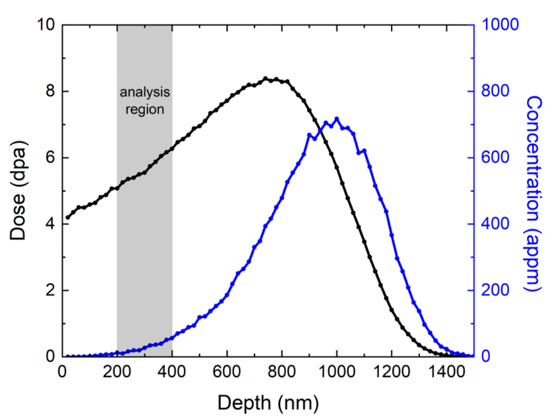

FIG. 8. SRIM simulated profile of the dose and ion concentration with respect to depth for Ni under 6 MeV I^{3+} irradiation.

APPENDIX B: CD SIMULATION UNDERPINNING THE DERIVATION

This section summarizes the CD simulation results that underpin the derivation of the quantitative relationship. Figure 9 shows that only small, TEM-invisible cavities exhibit significant thermal emission, whereas the thermal emission rate for larger cavities is negligible.

Figure 10 presents the effect of neglecting cavity size distribution: the CD model using the Fokker–Planck method incorporates the size distribution of TEM-visible cavities, while the mean-size approximation ignores it. The results indicate that the difference between the two approaches is minimal.

Figure 11 displays the evolution of defect density, revealing that defect nucleation occurs at low doses and essentially ceases at high doses. Consequently, the density of irradiation-induced defects can be approximated as constant during the cavity growth stage.

Figure 12 illustrates the contribution of defects of different sizes to the total irradiation-induced sink strength. At high doses, where cavity growth occurs, TEM-visible defects dominate, while the contribution from invisible small clusters is negligible.

Figure 13 presents the proportion of defect fluxes, indicating that point defects constitute the majority of the flux driving cavity growth.

Figure 14 demonstrates that an approximately proportional relationship exists between irradiation-induced defect density and dose rate, which holds across various temperatures. As discussed before, swelling occurs within a temperature window that shifts to higher temperatures with increasing dose rate; thus, for a given temperature, only a finite dose-rate window produces non-negligible swelling. Accordingly, a swelling level of 0.01% is taken as the lower bound for physically meaningful simulations.

Although sink strength has two components—defect density and size—the component enhanced by dose rate for nucleation remains dominant when the dose rate changes. This is reflected in the sink strength, which also

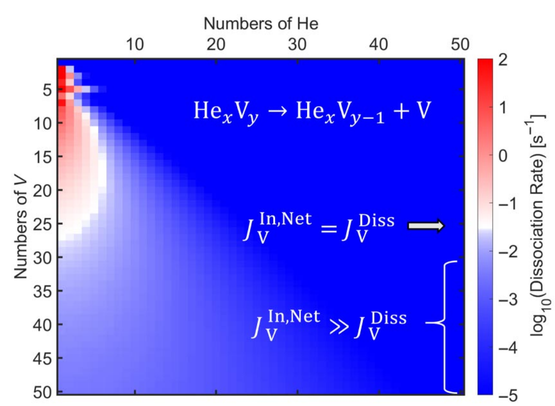

FIG. 9. Rate of thermal vacancy emission from cavities in BCC iron at 500 °C. $J_V^{In,Net}$ and J_V^{Diss} denote the net vacancy capture rate and the thermal emission rate of a cavity, respectively.

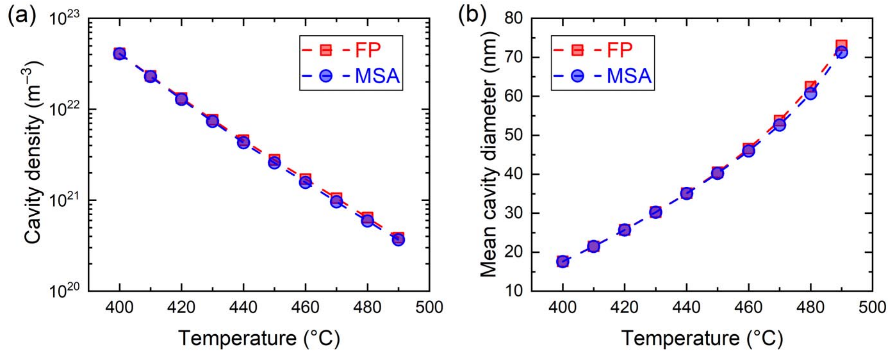

FIG. 10. Comparison between the cavity characteristics produced by the mean-size approximation (MSA) and the Fokker–Planck method (FP) in BCC iron. (a) Cavity density. (b) Cavity mean diameter. The irradiation dose is 50 dpa and the dose rate is 1×10^{-3} dpa/s.

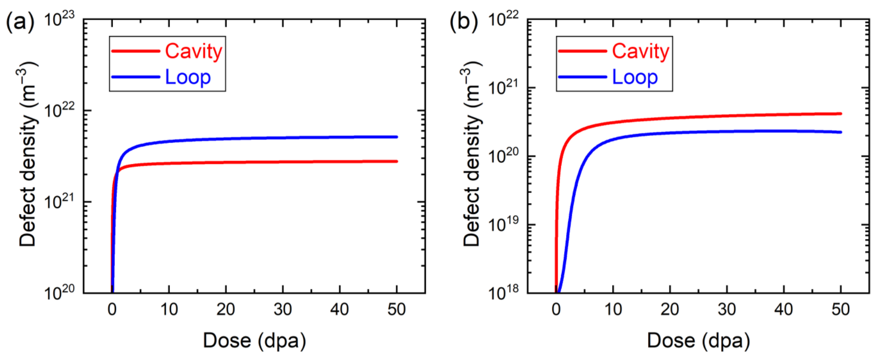

FIG. 11. Evolution of the densities of irradiation-induced dislocation loops and cavities with irradiation dose in BCC iron under typical ion and neutron irradiation conditions. (a) Ion irradiation condition: 1×10^{-3} dpa/s and 450 °C. (b) Neutron irradiation condition: 1×10^{-6} dpa/s and 340 °C.

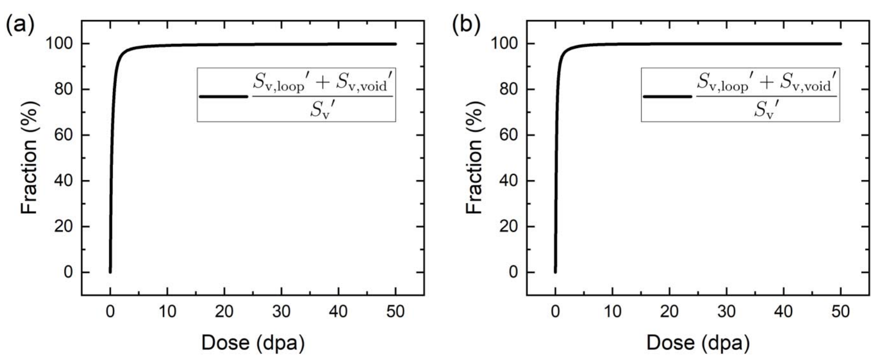

FIG. 12. Fraction of total irradiation-induced sink strength (S_{v}') from TEM-visible defects ($S_{\mathrm{v,loop}}' + S_{\mathrm{v,void}}'$) in BCC iron under typical ion and neutron irradiation conditions. (a) Ion irradiation condition: 1×10^{-3} dpa/s and 450 °C. (b) Neutron irradiation condition: 1×10^{-6} dpa/s and 340 °C.

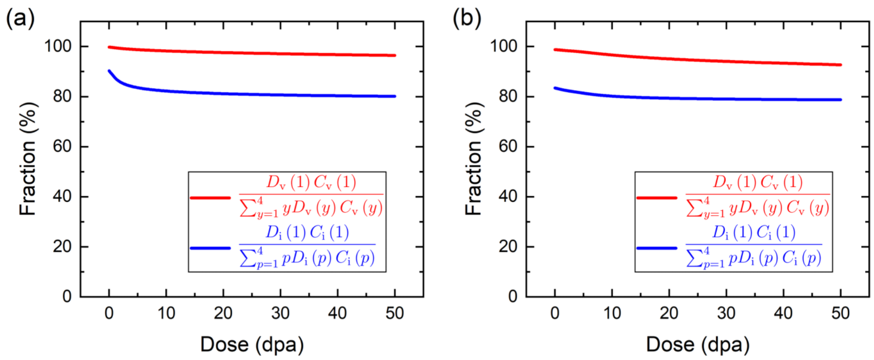

FIG. 13. Contribution of point defects to total defect flux in BCC iron under typical ion and neutron irradiation condition. (a) Ion irradiation conditions: 1×10^{-3} dpa/s and 450 °C. (b) Neutron irradiation condition: 1×10^{-6} dpa/s and 340 °C.

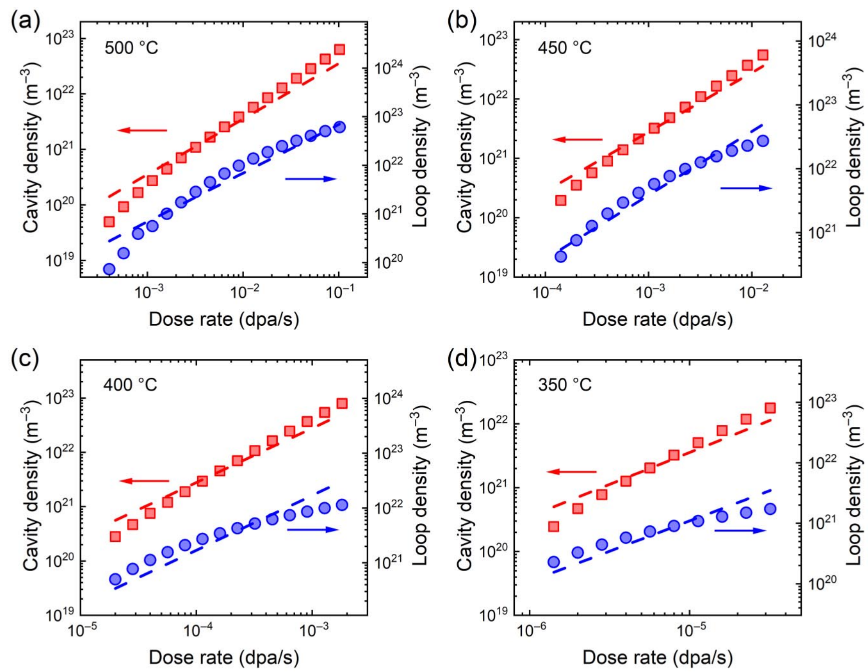

FIG. 14. Dose-rate dependence of irradiation-induced cavity and dislocation loop densities in BCC iron at 50 dpa for different temperatures. The alteration of defect density ρ with dose rate G_{dpa} is fitted to $\rho = \gamma G_{\mathrm{dpa}}$ (a) 500 °C. (b) 450 °C. (c) 400 °C. (d) 350 °C.

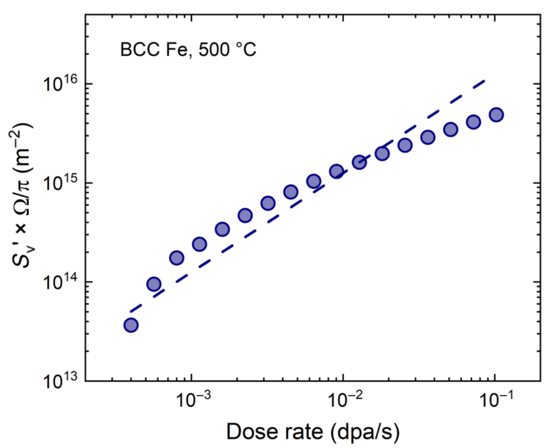

FIG. 15. Dose-rate dependence of sink strength at 500 °C and 50 dpa in BCC Fe. The alteration of defect density $S_v{}'$ with dose rate G_{dpa} is fitted to $S_v{}' = \delta_v G_{\mathrm{dpa}}$.

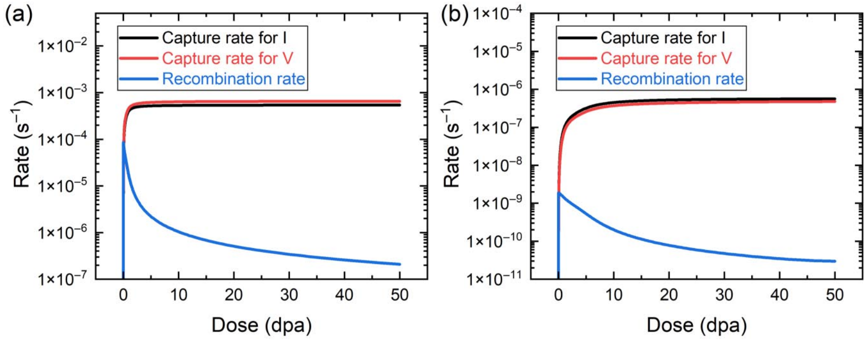

FIG. 16. Comparison between the recombination rate of displacement point defects and the capture rates of displacement point defects by sinks (clusters in the MSA size regime). (a) Ion irradiation condition: 1×10^{-3} dpa/s and 450 °C. (b) Neutron irradiation condition: 1×10^{-6} dpa/s and 340 °C.

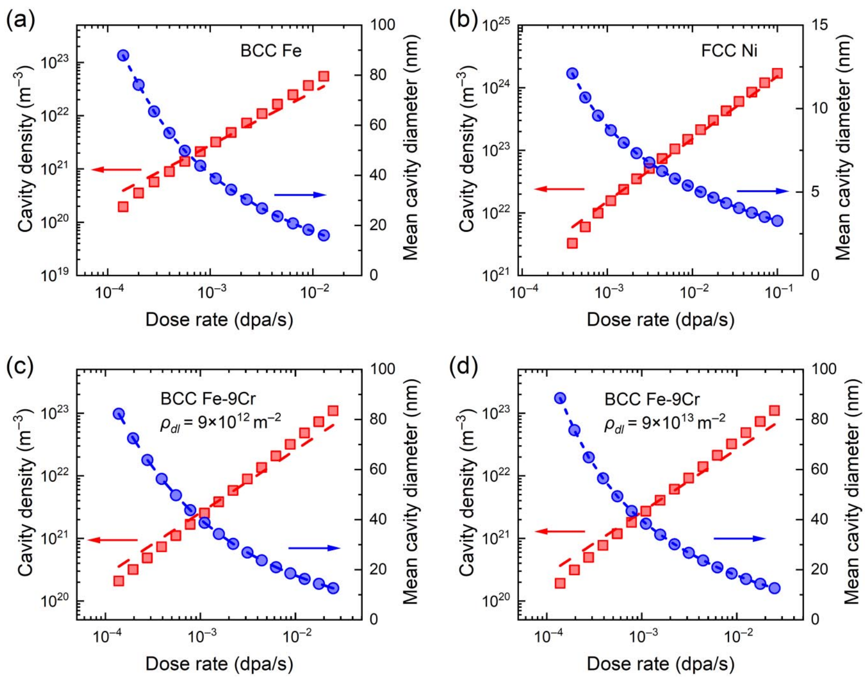

FIG. 17. Dose-rate dependence of cavity size and density at 450 °C and 50 dpa. The alteration of defect density ρ with dose rate G_{dpa} is fitted to $\rho = \gamma G_{\mathrm{dpa}}$ (a) BCC Fe. (b) FCC Ni and BCC Fe–9Cr with intrinsic dislocation densities of (c) 9×10^{12} m^{-2} (d) 9×10^{13} m^{-2}.

exhibits an approximate proportionality to the dose rate, as shown in Fig. 15.

Although a recombination term exists in the defect concentration equations, Fig. 16 indicates that this term is negligible at high doses.

Figure 17 further shows the variation in cavity density and size with dose rate. As expected, cavity size decreases with increasing dose rate. Moreover, the approximately proportional relationship between defect density and dose rate remains valid in FCC materials.

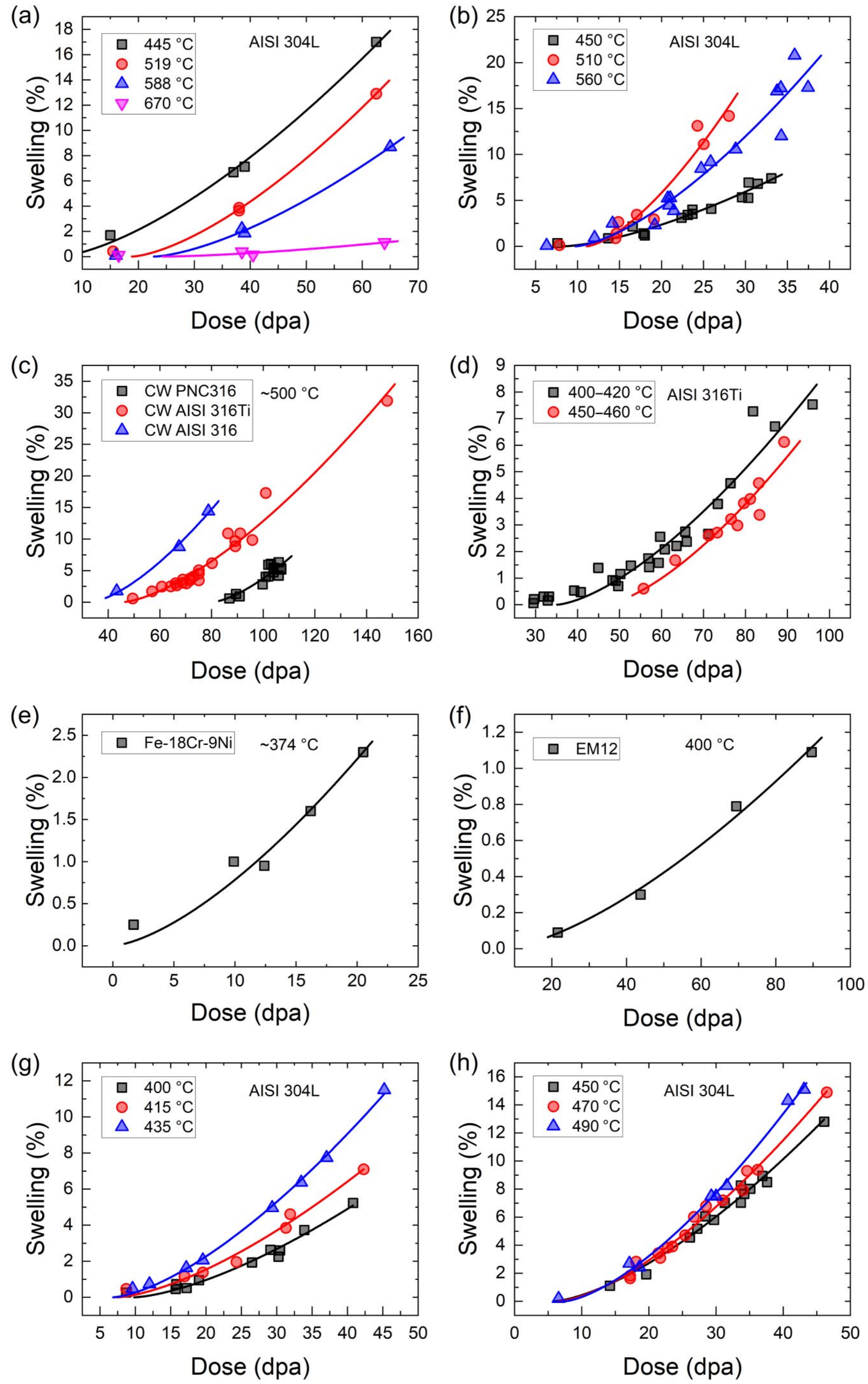

FIG. 18. Swelling induced by neutron irradiation in different materials under various conditions. (a) AISI 304L alloys at 445–670 °C [33], (b) AISI 304L alloys at 450–560 °C [33], (c) 20% cold-work 316 stainless steel at about 500 °C [41], (d) AISI 316Ti alloys in different temperature ranges [34], (e) Fe-18Cr-9Ni alloy at ~374 °C [40], (f) EM12 alloy at 400 °C [41], (g) AISI 304L alloys at 400–435 °C [33], and (h) AISI 304L alloys at 450–490 °C [33].

APPENDIX C: OTHER FITTING EXAMPLES

The relationship between cavity swelling and irradiation dose is further illustrated here. The neutron irradiation results, as shown in Fig. 18, along with the ion irradiation results presented in Fig. 19, demonstrate that the quantitative relationship accurately describes the dose dependence of swelling across different materials and temperatures.

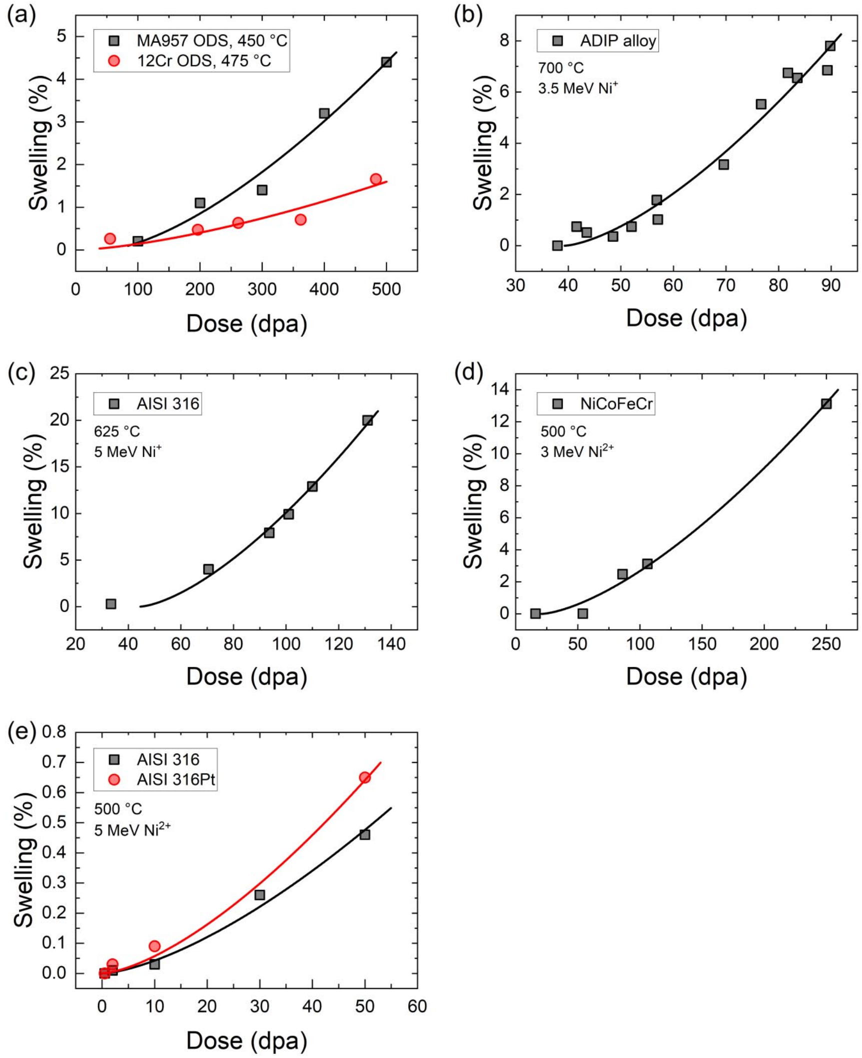

FIG. 19. Swelling induced by ion irradiation in different materials and under various conditions. (a) MA957 [42] and 12Cr ODS [43] alloys at 450 and 475 °C, respectively, (b) ADIP alloy at 700 °C [44], (c) AISI 316 at 625 °C [45], (d) NiCoFeCr at 500 °C [45], and (e) AISI 316 and AISI 316Pt alloys at 500 °C [46].

APPENDIX D: EFFECT OF HELIUM IN NEUTRON-IRRADIATED NICKEL

Ayanoglu *et al.* [27] reported a helium generation rate of 1appm He/dpa for a Fe-21Cr-32Ni austenitic alloy in the BOR-60 fast reactor. Based on this, the helium generation rate for pure nickel in BOR-60 is estimated to be 3 appm He/dpa. Accordingly, CD simulations of cavity evolution were performed at the corresponding neutron

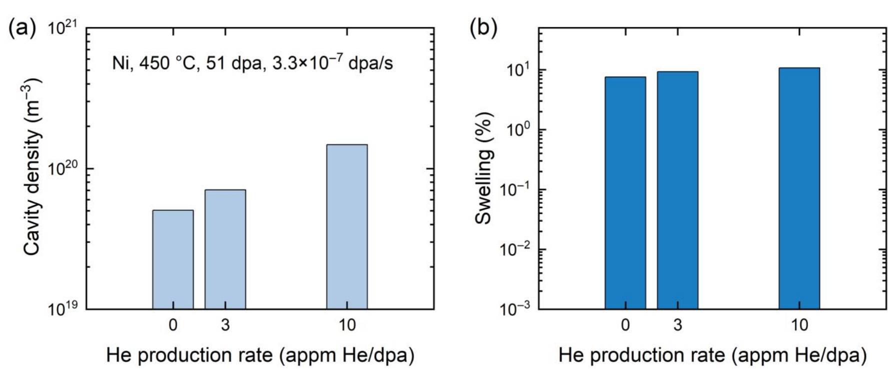

FIG. 20. Helium effects on (a) cavity density and (b) swelling in neutron-irradiated nickel obtained from CD simulations.

TABLE IV. Fitting parameters for Fig. 4.

	α'	k	c	d
AISI 304, 373–388 °C	29191974.90	336524735.6	24.127	2.958
Fe-15Cr-16Ni, ~400 °C	21843197.30	29533280.10	52.135	7.333
Fe-18Cr-10Ni-Ti, 590 °C	348675.809	470049.545	132.25	41.13
AISI 304L, ~500 °C	95966.135	129044.023	26.336	2.851
HT9, ~420 °C	611.707	53425.041	264.576	31.05

irradiation dose rate, considering both the helium-free condition and scenarios with 3 and 10 appm He/dpa (the latter accounting for uncertainty in the estimated helium generation rate). As anticipated, helium significantly enhanced cavity nucleation, leading to a marked increase in cavity number density as shown in Fig. 20(a). However, its impact on macroscopic swelling was minimal: at 3 appm He/dpa, the swelling increase was merely 23% compared to the helium-free case as shown in Fig. 20(b). This marginal effect is negligible when contrasted with the orders-of-magnitude difference in swelling induced by variations in dose rate.

APPENDIX E: FITTING PARAMETERS

Tables IV, V, and VI record the fitting parameters for Figs. 4 and 5. The uncertainties associated with TEM-characterized ion irradiation swelling data were addressed through Monte Carlo simulations (10,000 iterations) to evaluate their propagation to neutron irradiation predictions [83,84]. Each iteration involved: (1) random perturbation of mean experimental swelling values using normal distributions (standard deviation = measurement error), and (2) subsequent nonlinear least-squares fitting of the modified dataset.

TABLE V. Fitting parameters for Fig. 5(a).

	α	Δ_0
CW AISI 316, 500–525 °C	0.0754	20.39

TABLE VI. Fitting parameters for Fig. 5(b).

	α'	k	c	d
CW AISI 316, ~575 °C	132803.17	292979.83	162.74	22.01

TABLE VII. Fitting parameters and predicted swelling for Fig. 6. Prediction1: 38 dpa, 3.7×10^{-7} dpa/s; Prediction2: 51 dpa, 3.3×10^{-7} dpa/s.

	Mean	SD
α'	76921.09	22383.46
k	533603.59	44011.48
c	0.5234	1.0045
d	0.9586	0.3288
Prediction1	6.2197	1.2604
Prediction2	8.4462	1.8381

The incubation stage refers to the initial irradiation period characterized by extremely slow swelling growth. Consequently, the incubation dose in the formulation must explicitly satisfy the condition: $\Delta_0 = c + d\,\lg(G_{\mathrm{dpa}}) > 0$. It is critical to note that although the incubation dose decreases with reduced dose rates, the condition must be rigorously enforced when extrapolating ion irradiation data to predict neutron-induced swelling. In this work, parameter bounds were predefined prior to implementing the MATLAB function lsqcurvefit. From the experimental results, it is clear that the incubation dose should be less than 5 under ion irradiation conditions, while the incubation dose should be greater than 0 under neutron irradiation at the lowest dose rate, i.e.

$$\begin{cases} c + dlg\,(1.1\times10^{-2}) < 5 \\ c + dlg\,(3.3\times10^{-7}) > 0 \end{cases}. \tag{E1}$$

It yields a strict upper bound $d < 1.1055$. Coupled with the positive correlation between dose rate and incubation dose, the physically admissible domain is constrained to: $0 < d < 1.1055$. Using the method described above, the calculated fitting parameters and predicted values are listed in Table VII and plotted in Fig. 6.

For Fig. 7 the incubation dose is also required to have a clear physical meaning and therefore must remain positive. However, for materials that swell readily, the fitted incubation dose approaches zero, so that even small experimental uncertainties can lead to order-of-magnitude variations in the ratio Δ_0/α. To ensure numerical stability while preserving physical consistency, a lower bound of 0.1 dpa was imposed on the incubation dose during the fitting procedure for Fig. 7.

APPENDIX F: MANSUR'S INVARIANCE THEORY

Mansur's invariance theory posits that the higher dose rates typical of ion irradiation, relative to neutron irradiation, can be offset by an appropriate increase in the irradiation temperature. To establish equivalence between the two irradiation modalities, the irradiation variables

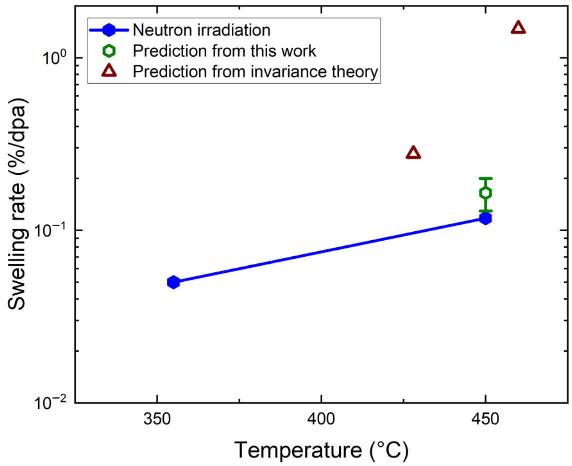

FIG. 21. Comparison between the present fixed-temperature prediction framework and Mansur's invariance-theory-based temperature-shift approach for pure Ni. The invariance-theory points are obtained from self-ion-irradiation data at 600 and 650 °C [102], which correspond to equivalent neutron-irradiation temperatures of 428 and 460 °C, respectively. The prediction from the present framework is obtained by fitting the 450 °C ion-irradiation data and predicting the neutron swelling rate at 450 °C under the corresponding neutron dose rate.

must satisfy the following relationship [23]:

$$T_{\text{ion}} - T_{\text{neutron}} = \frac{\frac{kT_{\text{neutron}}^2}{E_{\text{v}}^{\text{m}}+nE_{\text{v}}^{\text{f}}}\ln\left(\frac{G_{\text{ion}}}{G_{\text{neutron}}}\right)}{1-\frac{kT_{\text{neutron}}}{E_{\text{v}}^{\text{m}}+nE_{\text{v}}^{\text{f}}}\ln\left(\frac{G_{\text{ion}}}{G_{\text{neutron}}}\right)} \quad \text{(F1)}$$

where T is the irradiation temperature, G is the dose rate, k is Boltzmann's constant, and E_{v}^{m} and E_{f}^{v} are the vacancy migration and formation energies, respectively. The parameter n is determined by the dominant defect annihilation mechanism: $n = 1$ when the defect mutual recombination rate is much lower than the defect absorption rate at sinks, and $n = 2$ when the recombination rate is much higher than the sink absorption rate.

For pure Ni, the values of E_{v}^{m} and E_{f}^{v} are 1.04 and 1.79 eV, respectively [101]. As demonstrated previously, the rate of defect absorption by sinks vastly exceeds the mutual recombination rate during the cavity growth stage; thus, $n = 1$ is applied in this analysis.

Under an ion irradiation dose rate of approximately 3×10^{-3} dpa/s [102], pure Ni irradiated at 600°C to a dose of 20 dpa exhibits a swelling of 5.5%. Similarly, irradiation at 650°C to 12 dpa yields a swelling of 17.6%. Based on the invariance theory, the corresponding equivalent neutron irradiation temperatures for these two conditions are calculated to be 428 and 460 °C, respectively. For comparison with neutron-irradiation data, the swelling values are normalized by irradiation dose to obtain swelling rates.

The prediction from the present framework is obtained differently. Because the present model establishes a relationship between swelling, dose, and dose rate at a fixed temperature, the parameters are fitted using pure Ni ion-irradiation data at 450 °C and then used to predict neutron swelling at 450 °C directly. The prediction point shown in Fig. 21 corresponds to the predicted swelling at 51 dpa in Table III, normalized by the dose, namely 8.4% at 51 dpa.

[1] S. J. Zinkle and L. L. Snead, *Designing radiation resistance in materials for fusion energy*, Annu. Rev. Mater. Res. **44**, 241 (2014).
[2] M. J. Norgett, M. T. Robinson, and I. M. Torrens, *A proposed method of calculating displacement dose rates*, Nucl. Eng. Des. **33**, 50 (1975).
[3] Y. Lin, C. Lu, T. Yang, Z. Su, Y. Deng, W. Hu, H. Deng, G. Lu, and F. Gao, *Formation of voids or stacking-fault tetrahedra induced by local chemical variations in face-centered-cubic complex concentrated alloys*, Phys. Rev. Lett. **136**, 016102 (2026).
[4] S. J. Zinkle and G. S. Was, *Materials challenges in nuclear energy*, Acta Mater. **61**, 735 (2013).
[5] S. J. Zinkle and J. Steven, *Radiation-induced effects on microstructure*, in *Comprehensive Nuclear Materials* (2012), pp. 65–98, 10.1016/B978-0-08-056033-5.00003-3.
[6] R. F. Mattas, F. A. Garner, M. L. Grossbeck, P. J. Maziasz, G. R. Odette, and R. E. Stoller, *The impact of swelling on fusion reactor first wall lifetime*, J. Nucl. Mater. **122**, 230 (1984).
[7] C. Cawthorne and E. J. Fulton, *Voids in irradiated stainless steel*, Nature (London) **216**, 575 (1967).
[8] G. S. Was, *Fundamentals of Radiation Materials Science* (Springer, New York, 2017).
[9] W. Ge, S. Zhao, C. Wang, H. Liu, Y. Su, J. Huang, Z. Gao, J. Xue, and Y. Wang, *A model for dose dependence of the void swelling in electron-irradiated alloys*, Metals **12**, 244 (2022).
[10] S. J. Zinkle and K. Farrell, *Void swelling and defect cluster formation in reactor-irradiated copper*, J. Nucl. Mater. **168**, 262 (1989).
[11] F. A. Garner, *Radiation damage in austenitic steels*, in *Comprehensive Nuclear Materials* (Elsevier, New York, 2012), pp. 33–95.
[12] O. El-Atwani *et al.*, *Outstanding radiation resistance of tungsten-based high-entropy alloys*, Sci. Adv. **5**, eaav2002 (2019).
[13] F. Massee, P. O. Sprau, Y.-L. Wang, J. C. Séamus Davis, G. Ghigo, G. D. Gu, and W.-K. Kwok, *Imaging atomic-scale effects of high-energy ion irradiation on superconductivity and vortex pinning in* Fe(Se, Te), Sci. Adv. **1**, e1500033 (2015).
[14] S. Agarwal *et al.*, *A new mechanism for void-cascade interaction from nondestructive depth-resolved atomic-scale measurements of ion irradiation–induced defects in* Fe, Sci. Adv. **6**, eaba8437 (2020).

[15] J. G. Gigax, E. Aydogan, T. Chen, D. Chen, L. Shao, Y. Wu, W. Y. Lo, Y. Yang, and F. A. Garner, *The influence of ion beam rastering on the swelling of self-ion irradiated pure iron at* 450 °C, J. Nucl. Mater. **465**, 343 (2015).

[16] G. S. Was, *Challenges to the use of ion irradiation for emulating reactor irradiation*, J. Mater. Res. **30**, 1158 (2015).

[17] T. Okita and W. G. Wolfer, *A critical test of the classical rate theory for void swelling*, J. Nucl. Mater. **327**, 130 (2004).

[18] G. S. Was and R. S. Averback, *Radiation damage using ion beams*, (Elsevier, New York, 2012), pp. 195–221.

[19] S. J. Zinkle, *Advanced irradiation-resistant materials for generation IV nuclear reactors*, in *Structural Materials for Generation IV Nuclear Reactors*, edited by P. Yvon (Woodhead Publishing, 2017), pp. 569–594, 10.1016/B978-0-08-100906-2.00016-1.

[20] P. Hosemann, D. Kiener, Y. Wang, and S. A. Maloy, *Issues to consider using nano indentation on shallow ion beam irradiated materials*, J. Nucl. Mater. **425**, 136 (2012).

[21] S. J. Zinkle and L. L. Snead, *Opportunities and limitations for ion beams in radiation effects studies: Bridging critical gaps between charged particle and neutron irradiations*, Scr. Mater. **143**, 154 (2018).

[22] B. Zhang, F. Luo, Y. Liu, J. Wang, D. Chen, X. Guo, C. Wang, S. J. Zinkle, and Y. Wang, *Object kinetic Monte Carlo simulations on the difference between fission neutron and heavy ion irradiation induced void evolution in* Fe-Cr *alloys*, .

[23] L. K. Mansur, *Theory and experimental background on dimensional changes in irradiated alloys*, J. Nucl. Mater. **216**, 97 (1994).

[24] S. Taller, G. VanCoevering, B. D. Wirth, and G. S. Was, *Predicting structural material degradation in advanced nuclear reactors with ion irradiation*, Sci. Rep. **11**, 2949 (2021).

[25] G. S. Was, Z. Jiao, E. Getto, K. Sun, A. M. Monterrosa, S. A. Maloy, O. Anderoglu, B. H. Sencer, and M. Hackett, *Emulation of reactor irradiation damage using ion beams*, Scr. Mater. **88**, 33 (2014).

[26] G. S. Was *et al.*, *International round robin on ion irradiation of alloy T91 and comparison with neutron irradiation*, J. Nucl. Mater. **616**, 156065 (2025).

[27] M. Ayanoglu and A. T. Motta*Emulation of neutron-irradiated microstructure of austenitic 21Cr32Ni model alloy using dual-ion irradiation*, J. Nucl. Mater. **570**, 153944 (2022).

[28] M. R. Gilbert *et al.*, *Perspectives on multiscale modelling and experiments to accelerate materials development for fusion*, J. Nucl. Mater. **554**, 153113 (2021).

[29] S. I. Golubov, A. V. Barashev, and R. E. Stoller, *Reaction rate theory*, in *Comprehensive Nuclear Materials* (Elsevier, Oxford, 2020), pp. 717–753.

[30] A. A. Kohnert, B. D. Wirth, and L. Capolungo, *Modeling microstructural evolution in irradiated materials with cluster dynamics methods: A review*, Comput. Mater. Sci. **149**, 442 (2018).

[31] I. Martin-Bragado, A. Rivera, G. Valles, J. L. Gomez-Selles, and M. J. Caturla, *MMonCa: An object kinetic MonteCarlo simulator for damage irradiation evolution and defect diffusion*, Comput. Phys. Commun. **184**, 2703 (2013).

[32] F. A. Garner, M. B. Toloczko, and B. H. Sencer, *Comparison of swelling and irradiation creep behavior of fcc-austenitic and bcc-ferritic/martensitic alloys at high neutron exposure*, J. Nucl. Mater. **276**, 123 (2000).

[33] F. A. Garner and D. L. Porter, *A reassessment of the swelling behavior of AISI. 304 stainless steel*, in *Dimensional Stability and Mechanical Behaviour of Irradiated Metals and Alloys* (Thomas Telford Publishing, 1984), Vol. 2, pp. 41–44, https://www.emerald.com/books/edited-volume/17570/chapter-abstract/95899747/P8-A-reassessment-of-the-swelling-behavior-of-AISI?redirectedFrom=fulltext.

[34] P. Dubuisson, A. Maillard, C. Delalande, D. Gilbon, J.-L. Seran, A. Kumar Stoller, and D. Gelles, *The effect of phosphorus on the radiation-induced microstructure of stabilized austenitic stainless steels*, in *Effects of Radiation on Materials: 15th International Symposium*, edited by A. Kumar and D. Gelles (ASTM International, 1992), vol. STP1125-EB, 10.1520/STP17926S.

[35] A. S. Kalchenko, V. V. Bryk, N. P. Lazarev, I. M. Neklyudov, V. N. Voyevodin, and F. A. Garner, *Prediction of swelling of* 18Cr10NiTi *austenitic steel over a wide range of displacement rates*, J. Nucl. Mater. **399**, 114 (2010).

[36] C. Sun, F. A. Garner, L. Shao, X. Zhang, and S. A. Maloy, *Influence of injected interstitials on the void swelling in two structural variants of 304L stainless steel induced by self-ion irradiation at* 500 °C, Nucl. Instrum. Methods Phys. Res. Sect. B Beam Interact. Mater. At. **409**, 323 (2017).

[37] B. Makenas, *Swelling of 20% cold-worked type 316 stainless steel fuel pin cladding and ducts*, in *Effects of Radiation on Materials: Twelfth International Symposium* (ASTM International, West Conshohocken, PA, 1985), pp. 202–211.

[38] H. Kim, J. G. Gigax, J. Fan, F. A. Garner, T.-L. Sham, and L. Shao, *Swelling resistance of advanced austenitic alloy A709 and its comparison with 316 stainless steel at high damage levels*, J. Nucl. Mater. **527**, 151818 (2019).

[39] S. Ukai and T. Uwaba, *Swelling rate versus swelling correlation in 20% cold-worked 316 stainless steels*, J. Nucl. Mater. **317**, 93 (2003).

[40] E. N. Shcherbakov *et al.*, *Influence of damage rate on physical and mechanical properties and swelling of* 18Cr−9Ni *austenitic steel in the range of* 3×10^{-9} *to* 4×10^{-8} dpa/s, J. Nucl. Mater **386–388**, 152 (2009).

[41] P. Dubuisson, D. Gilbon, and J. L. Séran, *Microstructural evolution of ferritic-martensitic steels irradiated in the fast breeder reactor Phénix*, J. Nucl. Mater. **205**, 178 (1993).

[42] M. B. Toloczko, F. A. Garner, V. N. Voyevodin, V. V. Bryk, O. V. Borodin, V. V. Mel'nychenko, and A. S. Kalchenko, *Ion-induced swelling of ODS ferritic alloy MA957 tubing to 500 dpa*, J. Nucl. Mater. **453**, 323 (2014).

[43] T. Chen, E. Aydogan, J. G. Gigax, D. Chen, J. Wang, X. Wang, S. Ukai, F. A. Garner, and L. Shao, *Microstructural changes and void swelling of a 12Cr ODS ferritic-martensitic alloy after high-dpa self-ion irradiation*, J. Nucl. Mater. **467**, 42 (2015).

[44] F. A. Garner, *Impact of the injected interstitial on the correlation of charged particle and neutron-induced radiation damage*, J. Nucl. Mater. **117**, 177 (1983).

[45] W. G. Johnston, J. H. Rosolowski, A. M. Turkalo, and T. Lauritzen, *An experimental survey of swelling in commercial Fe-Cr-Ni alloys bombarded with 5 MeV Ni ions*, J. Nucl. Mater. **54**, 24 (1974).

[46] J. Gan, E. P. Simonen, S. M. Bruemmer, L. Fournier, B. H. Sencer, and G. S. Was, *The effect of oversized solute additions on the microstructure of 316SS irradiated with* 5MeV Ni^{++} *ions or 3.2 MeV protons*, J. Nucl. Mater. **325**, 94 (2004).

[47] Y. Watanabe, K. Morishita, T. Nozawa, and H. Tanigawa, *Irradiation temperature and dose rate dependence of void swelling in RAFM steel during irradiation: Reaction rate theory analysis*, Fusion Eng. Des. **194**, 113899 (2023).

[48] J. Gao, E. Gaganidze, B. Kaiser, and J. Aktaa, *Integrated modeling of helium-vacancy clustering in Eurofer97 steel upon* He^{+}/Fe^{3+} *dual-beam irradiation*, J. Nucl. Mater **547**, 152822 (2021).

[49] T. Jourdan, G. Bencteux, and G. Adjanor, *Efficient simulation of kinetics of radiation induced defects: A cluster dynamics approach*, J. Nucl. Mater. **444**, 298 (2014).

[50] A. Gokhman and F. Bergner, *Cluster dynamics simulation of point defect clusters in neutron irradiated pure iron*, Radiat. Eff. Defects Solids **165**, 216 (2010).

[51] Y. Watanabe, H. Iwakiri, N. Yoshida, K. Morishita, and A. Kohyama, *Formation of interstitial loops in tungsten under helium ion irradiation: Rate theory modeling and experiment*, Nucl. Instrum. Methods Phys. Res., Sect. B **255**, 32 (2007).

[52] Y. Xiong, J. Zhang, S. Ma, S. Huang, B. Xu, and S. Zhao, *Multiscale modeling of irradiation-induced defect evolution in BCC multi principal element alloys*, J. Alloys Compd. **953**, 170084 (2023).

[53] M. Chiapetto, L. Malerba, and C. S. Becquart, *Effect of Cr content on the nanostructural evolution of irradiated ferritic/martensitic alloys: An object kinetic Monte Carlo model*, J. Nucl. Mater. **465**, 326 (2015).

[54] S. Plimpton, *Fast parallel algorithms for short-range molecular dynamics*, J. Comput. Phys. **117**, 1 (1995).

[55] G. Bonny, N. Castin, and D. Terentyev, *Interatomic potential for studying ageing under irradiation in stainless steels: The* FeNiCr *model alloy*, Model. Simul. Mater. Sci. Eng. **21**, 085004 (2013).

[56] D. Brimbal, L. Fournier, and A. Barbu, *Cluster dynamics modeling of the effect of high dose irradiation and helium on the microstructure of austenitic stainless steels*, J. Nucl. Mater. **468**, 124 (2016).

[57] U. Saha, A. Dutta, C. Konkati, S. Chakraborty, S. Dey, A. Chauhan, S. Srivastava, N. Gayathri, and P. Mukherjee, *Microstructure and defect evolution in oxygen ion-irradiated pure nickel: Insights from experimental probes and molecular dynamics simulations*, Mater. Chem. Phys. **305**, 127916 (2023).

[58] J. J. Hoyt and F. A. Garner, *The solute dependence of bias factors in irradiated Fe–Ni alloys*, J. Nucl. Mater. **179–181**, 1096 (1991).

[59] L. Malerba, *Molecular dynamics simulation of displacement cascades in* α*-Fe: A critical review*, J. Nucl. Mater. **351**, 28 (2006).

[60] A. Souidi, M. Hou, C. S. Becquart, L. Malerba, C. Domain, and R. E. Stoller, *On the correlation between primary damage and long-term nanostructural evolution in iron under irradiation*, J. Nucl. Mater. **419**, 122 (2011).

[61] F. Luo, B. Zhang, Z. Gao, J. Huang, H.-B. Zhou, G.-H. Lu, F. Gao, Y. Wang, and C. Wang, *Quantitative method to predict the energetics of helium-nanocavities interactions in metal systems based on electrophobic interaction*, J. Materiomics **10**, 725 (2024).

[62] K. Ferasat, I. Martin-Bragado, Z. Yao, and L. K. Béland, *He bubble growth in nickel simulated by object kinetic Monte Carlo*, J. Nucl. Mater. **576**, 154231 (2023).

[63] Y. Watanabe, K. Morishita, T. Nozawa, and H. Tanigawa, *Size and temperature dependence of the point defect binding free energy to defect clusters in bcc* Fe, Plasma Fusion Res. **17**, 1205105 (2022).

[64] C.-C. Fu, J. D. Torre, F. Willaime, J.-L. Bocquet, and A. Barbu, *Multiscale modelling of defect kinetics in irradiated iron*, Nat. Mater. **4**, 68 (2005).

[65] A. Iwase, T. Iwata, S. Sasaki, and T. Nihira, *Radiation annealing in nickel and copper by 100 MeV iodine ions*, J. Phys. Soc. Jpn. **59**, 1451 (1990).

[66] J. Huang *et al.*, *Effect of damage rate on the cavity swelling of pure nickel irradiated with triple ion beams*, Metals **12**, 7 (2022).

[67] H. Watanabe, A. Aoki, H. Murakami, T. Muroga, and N. Yoshida, *Effects of phosphorus on defect behavior, solute segregation and void swelling in electron irradiated Fe-Cr-Ni alloys*, J. Nucl. Mater. **155–157**, 815 (1988).

[68] T. Muroga, H. Watanabe, and N. Yoshida, *Correlation of fast neutron, fusion neutron and electron irradiations based on the dislocation loop density*, J. Nucl. Mater. **174**, 282 (1990).

[69] W. Chrominski, L. Ciupinski, P. Bazarnik, S. Markelj, and T. Schwarz-Selinger, *TEM investigation of the influence of dose rate on radiation damage and deuterium retention in tungsten*, Mater. Charact. **154**, 1 (2019).

[70] Z. Cao, Y. Ding, Q. Zhong, M. Wu, and G. Ran, *Defect evolution in Fe using in-situ Fe-H-He triple-beam simultaneous irradiation under two orders of magnitude of dose rates with constant H/dpa and he/dpa ratios*, J. Nucl. Mater. **617**, 156157 (2025).

[71] Y. Ding, G. Ran, Y. Li, Z. Cao, D. Cui, J. Huang, and Z. Zhou, *Effect of dose rate on dislocation loop evolution in tungsten: Combination of defect generation rate and elastic interaction*, Scr. Mater. **222**, 115054 (2023).

[72] M. P. Surh, J. B. Sturgeon, and W. G. Wolfer, *Radiation swelling behavior and its dependence on temperature, dose rate, and dislocation structure evolution*, J. Nucl. Mater. **336**, 217 (2005).

[73] S. I. Golubov, A. M. Ovcharenko, A. V. Barashev, and B. N. Singh, *Grouping method for the approximate solution of a kinetic equation describing the evolution of point-defect clusters*, Philos. Mag. A **81**, 643 (2001).

[74] M. Kiritani, *Analysis of the clustering process of supersaturated lattice vacancies*, J. Phys. Soc. Jpn. **35**, 95 (1973).

[75] J. Gan and G. S. Was, *Microstructure evolution in austenitic Fe–Cr–Ni alloys irradiated with rotons: comparison with neutron-irradiated microstructures*, J. Nucl. Mater. **297**, 161 (2001).
[76] M. Kiritani, *Microstructure evolution during irradiation*, J. Nucl. Mater. **216**, 220 (1994).
[77] C. Pokor, Y. Brechet, P. Dubuisson, J.-P. Massoud, and A. Barbu, *Irradiation damage in 304 and 316 stainless steels: Experimental investigation and modeling. Part I: Evolution of the microstructure*, J. Nucl. Mater. **326**, 19 (2004).
[78] R. E. Stoller and G. R. Odette, *Composite model of microstructural evolution in austenitic stainless steel under fast neutron irradiation, Oak Ridge National Lab., TN (USA). Metals and Ceramics Div*, Oak Ridge National Lab., TN (USA). Metals and Ceramics Div.; California Univ., Santa Barbara (USA), No. CONF-860605-28, 1986.
[79] M. B. Toloczko and F. A. Garner, *Irradiation creep and void swelling of two LMR heats of HT9 at* ~400 °C *and 165 dpa*, J. Nucl. Mater **233–237**, 289 (1996).
[80] B. H. Sencer, J. R. Kennedy, J. I. Cole, S. A. Maloy, and F. A. Garner, *Microstructural analysis of an HT9 fuel assembly duct irradiated in FFTF to 155 dpa at 443 °C*, J. Nucl. Mater. **393**, 235 (2009).
[81] D. S. Gelles, *Microstructural examination of commercial ferritic alloys at 200 dpa*, J. Nucl. Mater **233–237**, 293 (1996).
[82] H. Kim, J. G. Gigax, C. J. Rietema, O. E. Atwani, M. R. Chancey, J. K. Baldwin, Y. Wang, and S. A. Maloy, *Void swelling of conventional and composition engineered HT9 alloys after high-dose self-ion irradiation*, J. Nucl. Mater. **560**, 153492 (2022).
[83] D. Rochman, A. Vasiliev, H. Ferroukhi, T. Zhu, S. C. van der Marck, and A. J. Koning, *Nuclear data uncertainty for criticality-safety: Monte Carlo vs linear perturbation*, Ann. Nucl. Energy **92**, 150 (2016).
[84] G. Khirich, *A Monte Carlo method for analyzing systematic and random uncertainty in quantitative nuclear magnetic resonance measurements*, Anal. Chem. **93**, 10039 (2021).
[85] N. I. Budylkin, E. G. Mironova, V. M. Chernov, V. A. Krasnoselov, S. I. Porollo, and F. A. Garner, *Neutron-induced swelling and embrittlement of pure iron and pure nickel irradiated in the BN-350 and BOR-60 fast reactors*, J. Nucl. Mater. **375**, 359 (2008).
[86] T. Okita, T. Sato, N. Sekimura, T. Iwai, and F. A. Garner, *The synergistic influence of temperature and displacement rate on microstructural evolution of ion-irradiated Fe–15Cr–16Ni model austenitic alloy*, J. Nucl. Mater. **367–370**, 930 (2007).
[87] K. C. Russell, *Nucleation of voids in irradiated metals*, Acta Metall. **19**, 753 (1971).
[88] W. G. Wolfer, *Advances in void swelling and helium bubble physics*, J. Nucl. Mater. **122**, 367 (1984).
[89] A. Zhong, C. Lapointe, A. M. Goryaeva, K. Arakawa, M. Athènes, and M.-C. Marinica, *Unraveling temperature-induced vacancy clustering in tungsten: From direct microscopy to atomistic insights via data-driven Bayesian sampling*, PRX Energy **4**, 013008 (2025).
[90] L. K. Mansur, *Correlation of neutron and heavy-ion damage: II. The predicted temperature shift if swelling with changes in radiation dose rate*, J. Nucl. Mater. **78**, 156 (1978).
[91] S. J. Zinkle, A. Möslang, T. Muroga, and H. Tanigawa, *Multimodal options for materials research to advance the basis for fusion energy in the ITER era*, Nucl. Fusion **53**, 104024 (2013).
[92] J. J. Holmes, *Irradiation-induced swelling In nickel alloys*, Trans. Am. Nucl. Soc. **12**, 117 (1969), https://www.osti.gov/biblio/4769436.
[93] S. J. Zinkle, J. L. Boutard, D. T. Hoelzer, A. Kimura, R. Lindau, G. R. Odette, M. Rieth, L. Tan, and H. Tanigawa, *Development of next generation tempered and ODS reduced activation ferritic/martensitic steels for fusion energy applications*, Nucl. Fusion **57**, 092005 (2017).
[94] S. Hiwatashi, Y. Kohno, K. Asakura, and A. Kohyama, *Microstructural developments in* Fe-Cr-W *low activation ferritic steels under dual beam charged particle irradiation*, J. Nucl. Mater. **179–181**, 709 (1991).
[95] A. Bhattacharya and S. J. Zinkle, *Cavity swelling in irradiated materials*, in *Comprehensive Nuclear Materials* (2020), pp. 406–455, 10.1016/B978-0-12-803581-8.11599-1.
[96] G. S. Was, *Irradiation-induced voids and bubbles*, in *Fundamentals of Radiation Materials Science* (2017), pp. 379–484), 10.1007/978-1-4939-3438-6_8.
[97] S. J. Zinkle, *1.03 - radiation-induced effects on microstructure**Prepared for the Oak Ridge National Laboratory under contract no. DE-AC05-000R22725*, in *Comprehensive Nuclear Materials*, edited by R. J. M. Konings (Elsevier, Oxford, 2012).
[98] A. S. Kalchenko, V. V. Bryk, N. P. Lazarev, V. N. Voyevodin, and F. A. Garner, *Prediction of void swelling in the baffle ring of WWER-1000 reactors for service life of 30-60 years*, J. Nucl. Mater. **437**, 415 (2013).
[99] J. Du, S. Jiang, P. Cao, C. Xu, Y. Wu, H. Chen, E. Fu, and Z. Lu, *Superior radiation tolerance via reversible disordering–ordering transition of coherent superlattices*, Nat. Mater. **22**, 442 (2023).
[100] R. E. Stoller, M. B. Toloczko, G. S. Was, A. G. Certain, S. Dwaraknath, and F. A. Garner, *On the use of SRIM for computing radiation damage exposure*, Nucl. Instrum. Methods Phys. Res. Sect. B Beam Interact. Mater. At. **310**, 75 (2013).
[101] S.-L. Shang, B.-C. Zhou, W. Y. Wang, A. J. Ross, X. L. Liu, Y.-J. Hu, H.-Z. Fang, Y. Wang, and Z.-K. Liu, *A comprehensive first-principles study of pure elements: Vacancy formation and migration energies and self-diffusion coefficients*, Acta Mater. **109**, 128 (2016).
[102] R. F. Pinizzotto, L. J. Chen, and A. J. Ardell, *Nickel and nitrogen ion irradiation induced void swelling and defect microstructures in* Ni-Al, Ni-Cr *and* Ni-Ti *solid solutions*, Metall. Trans. A **9**, 1715 (1978).